Structures 55 (2023) 587–605

Contents lists available at ScienceDirect

Structures

journal homepage: www.elsevier.com/locate/structures

Dynamic amplification of multi-span simply-supported prestressed concrete girder viaducts subjected to multi-body heavy vehicles

Shiyi Mei [a], Colin Caprani [a,*], Daniel Cantero [b]

[a] Department of Civil Engineering, Monash University, Melbourne, Victoria, Australia
[b] Department of Structural Engineering, Norwegian University of Science & Technology NTNU, Trondheim, Norway

A B S T R A C T

High productivity freight vehicles (HPFVs) are used in many countries to address increasing freight demand. However, it is then necessary to assess the safety of existing bridge structures subjected to HPFVs because of their increasing mass and dimension. A critical part of this work is to assess the dynamic amplification of such vehicles, without undue conservatism, often based on vehicle–bridge interaction (VBI) modelling. In the VBI problem, the vehicle model is usually derived using the Principle of Virtual Work or Euler–Lagrange methods. However, HPFVs are characterized by multiple bodies and articulation points and these techniques quickly become intractable. Alongside the vehicle model, the bridge is often assumed to be a single simply-supported span, or a few continuous spans, whereas many urban bridge viaducts, in particular, have multiple prestressed concrete (PSC) girder simply-supported spans. Furthermore, these bridges typically have an upwards hog as a result of the prestress and it is hypothesized that certain combinations of vehicle, hog, span length, and number of spans, could produce a large dynamic amplification of static load effects. In this work, Kane's Method is applied to heavy vehicle with multi-trailers combinations which provides a relatively easy, systematic, and numerical manipulation means of determining the vehicle dynamic equations. The 9-axle B-Double vehicle, common in Australia, is used as an example to illustrate the procedure of deriving the vehicle dynamic equations. We apply the resulting vehicle models in a comprehensive VBI model to consider the dynamic amplification of PSC girder viaducts. The results indicate that the studied PSC girder viaducts experience higher amplification than the equivalent single-span simply-supported bridges. Recommendations for future studies and practice, such as the number of spans in the viaduct to obtain the 'convergence' of dynamic amplification, are given.

1. Introduction

Due to the continuously growing freight demand, many countries have introduced high productivity freight vehicles (HPFVs) to accommodate the increasing freight demand. The large freight capacity of HPFVs, such as semi-trailers and B-doubles, can improve the transport efficiency by reducing the vehicle volumes for a given freight task. The B-double is a common HPFV type with a prime mover and two trailers in Australia, South Africa, and is increasingly used in Europe [1]. According to the Truck Impact Chart published by the Australian Trucking Association [2], heavier vehicles with more trailers reduce the number of trips, consume less fuel, release less carbon dioxide, and are a safer alternative compared with traditional freight vehicles, such as semi-trailers. However, not all existing bridges can provide safe access to HPFVs due to the larger mass and dimensions, especially for heavy trucks of complex configuration with tractor and trailers. A critical aspect of the assessment of existing bridges, and the design of new bridges, for such new vehicle configurations, is the Dynamic Amplification Factor (DAF) [3], defined as:

$$\mathrm{DAF} = \frac{\varepsilon_{\mathrm{T}}}{\varepsilon_{\mathrm{S}}}, \tag{1}$$

where ε_{T} is the maximum total load effect (e.g. bending moment) considering both the static and dynamic effects, and ε_{S} is the maximum static-only equivalent load effect noted during the traverse at mid-span [4–6]. Consequently, the evaluation of the DAF for these truck-trailer combinations for the entire bridge stock is vital for ensuring optimal freight productivity and structural safety.

In the Vehicle–Bridge-Interaction (VBI) problem, the dynamic equations of the bridge and vehicle can be derived separately and coupled by the compatibility conditions at the contact points between vehicle tyres and bridge surface [7]. This very useful separation of the vehicle and bridge models, allows for high-fidelity modelling of each component separately.

The simply supported beam is widely used to study the dynamic response of the bridge subject to external force. The one-dimensional (1-D) beam can be modelled by finite element method (FEM) with both vertical translation and rotation on each node [8,9]. Nikkhoo et al. [10] considered the simply supported bridge as a 2-D plate element, and simulated a vehicle meeting event by two series of moving inertial loads. González [11] made a literature review on VBI and indicated that bridges can be modelled by 2-D plate and grillage and three-dimensional (3-D) solid elements by using FEM. A continuous

* Corresponding author.
E-mail addresses: shiyi.mei1@monash.edu (S. Mei), colin.caprani@monash.edu (C. Caprani), daniel.cantero@ntnu.no (D. Cantero).

https://doi.org/10.1016/j.istruc.2023.05.125
Received 26 October 2022; Accepted 28 May 2023
Available online 19 June 2023

3-span bridge was examined by Zhu & Law [12] using the Rayleigh–Ritz method in which the bridge deck is simulated as an orthotropic thin rectangular plate. Liu et al. [13] investigated the impact effect of extra heavy vehicle on the continuous finite beam element bridge. Rezaiguia and Laefer [14] proposed a semi-analytical solution of continuous multi-span bridge decks by modal superposition, and they also suggested [15] the dynamic response of the model matches with that of Rayleigh–Ritz and finite element models.

Prestressed concrete bridges are extensively used in highway bridge networks. The time-dependent camber of the PSC beam is influenced by factors such as creep, shrinkage, and the loss of prestress force [16]. Indeed, the Australian code AS 5100.5 [17] requires an upward camber (hog) at long-term to avoid an undesirable sag deflection under permanent loads. This is not unique as, for example, the existence of hog deflections is an important consideration in the serviceability of high-speed rail bridges [18]. It is interesting then, that even though a variety of types of bridge models have been considered in VBI studies, the hog, a basic characteristic of PSC girders, has not been explicitly considered [19]. Finally, although many bridges or viaducts are multiple-span and simply-supported (especially in urban areas), this form of bridge structure has not yet been examined.

In previous VBI investigations, a wide variety of sprung vehicle models have been used to simulate heavy-vehicles. The truck with rigid configuration can be simulated as a half-car planar model [8] or extended to three dimensions allowing for roll rotation [12,20]. Kirkegaard et al. [21] derived a 6-axle articulated heavy lorry to study the interaction between heavy vehicles and highway bridges. Cantero et al. [22] provided generic equations of motions of articulated track-trailer configurations. Meyer et al. [9] applied a long multi-trailer heavy B-double vehicle with two articulations and seven axles configuration. However, all of these vehicle models were derived using the Principle of Virtual Work or Euler–Lagrange methods, which require *a priori* a choice of the dependent quantities. Consequently, these methods become increasingly intractable as more trailer bodies or different types of trailers with axle configuration [23] are introduced to satisfy the specific freight loading. Thus, there is a need for a general way of modelling such vehicles, that can be automated. Indeed, this problem has been previously recognized by Cantero [24], but has yet to be addressed through a single comprehensive modelling methodology.

This paper addresses the combined problem of the development of the heavy-vehicle dynamic model, and the analysis of PSC girder viaducts. A novel approach deriving equations of motion of heavy vehicle by using Kane's method [25] is introduced in Section 2. The typical Australian 9-axle B-double truck is set as an example to show the derivation procedure, and this method can be easily applied to rigid trucks, semi-trailers, and other types of more complicated tractor-trailer combinations. Comparison is made to previous multi-body vehicle models in literature as validation. In Section 3, the simply-supported bridge with hog is simulated by using superposition technique, where the hog is added to the road profile. The coupled VBI considering hog is presented and validated by comparing the dynamic bending moment and acceleration at the mid-span with a previous study. In Section 4, a numerical experiment is carried out to explore the influence of hog, vehicle velocity, and bridge span length on the simply supported bridge. Then, a multi-span simply-supported viaduct is examined in detail and discussed in Section 5. Finally, the maximum dynamic amplification of fifteen types of viaducts from one to fifteen spans are considered to investigate the distinction of DAF between single- and multi-span simply-supported viaducts in Section 6. It suggests the number of spans in the viaduct to obtain the 'convergence' of amplification.

2. Vehicle model

Kane's method – also known as the Lagrange form of d'Alembert's principle [26] – is often applied in the field of multi-body dynamics. For example, Pal [27] derived the underslung dynamic equations of a helicopter connecting multiple rigid bodies by cables and Gomez et al. [28] developed the mathematical model of a rotor-centrifugal-pendulum-vibration-absorber system. However, Kane's method has not been applied to derive the multi-body vehicle models in the VBI problem, most likely because it is only in recent years that multi-body vehicles have been studied in this field, as noted previously. For multi-body dynamic problems, compared with the virtual work and Euler–Lagrange methods, Kane's method provides a simpler way to derive these equations, through the introduction of partial velocities and accelerations. The method facilitates automation and numerical manipulation [29], and so is less error-prone [30] and has an open-source mature application [31]. Thus it is highly-suited for the multi-body systems characteristic of HPFVs.

The general procedure of deriving heavy vehicle's equations of motion using Kane's method is shown in Fig. 1 and the steps are:

- Specify the vehicle's geometry and define the masses of the tractor, trailers, and axles. In doing so, usually large bodies like the tractor and trailers are assumed as rigid bodies with both displacement and rotation considered, while the axle is often taken as a particle when its rotational motion is negligible. With this, the DOFs corresponding to the translational and rotational motions in the system can be defined and described as generalized coordinates q_j. The generalized velocity $u_j = \dot{q}_j$ is the first derivative of q_j with respect to time.
- Set local frames for rigid bodies and define the inertial (Newtonian) frame N, where the orientation of local frames is described by the rotations of rigid bodies.
- Describe the position, velocity v, acceleration a and angular velocity ω and acceleration α of joints and the centre of mass of tractor, trailers and axles in the inertial frame. Then generate the partial velocities and partial angular velocities of the rigid bodies and particles, ${}^N\tilde{v}^*$. The articulation joints between trailer bodies give nonholonomic constraints to reduce the number of DOF and the dependent generalized quantities q_r, u_r and $\dot{u}_r$ are replaced by other selected independent quantities.
- Determine the contacting forces $\mathbf{R}$, torques $\mathbf{T}$, and inertial forces $\mathbf{T}^*$ applied to the tractor, trailers, and axles.
- Based on the contact and inertial forces, $\tilde{v}^*$ and $\tilde{\omega}$, generate the generalized active force $\tilde{F}_i$ and inertial force $\tilde{F}_i^*$. The number of $\tilde{F}_i$ or $\tilde{F}_i^*$ equals to the number of independent generalized coordinates q_i and the ith partial velocity and angular velocity are defined by the coefficient for generalized velocity u_i.
- Finally, Kane's dynamic equation can be obtained from $\tilde{F}_i$ and $\tilde{F}_i^*$ from which, after linearization, the equation of motion of vehicle can be presented in matrix form.

In this paper, the typical 9-axle B-Double heavy vehicle in Australia is used as an application example to show the procedure of deriving the vehicle model using Kane's method. However, the method demonstrated here can be generally applied to other types of vehicles and tractor-trailer combinations. The dynamic prototype of a 9-axle B-Double vehicle is illustrated in Fig. 2, and the vehicle consists of one tractor, two semi-trailers, and 9 axles. The tractor and trailers are simulated as lumped mass rigid bodies, and the axles are considered as concentrated mass particles. The tractor and trailers are connected to the axle masses by the suspension system, and the axle is supported by the tyre system above the road surface. Both suspension and tyre systems are assumed only to provide compression and tensile forces, which are always parallel to the vertical axis. Note that all dimensions are measured relative to the module axis origin, e.g. the s_i are positive quantities, the r_i are negative quantities, and l_i are a mixture, but mostly negative.

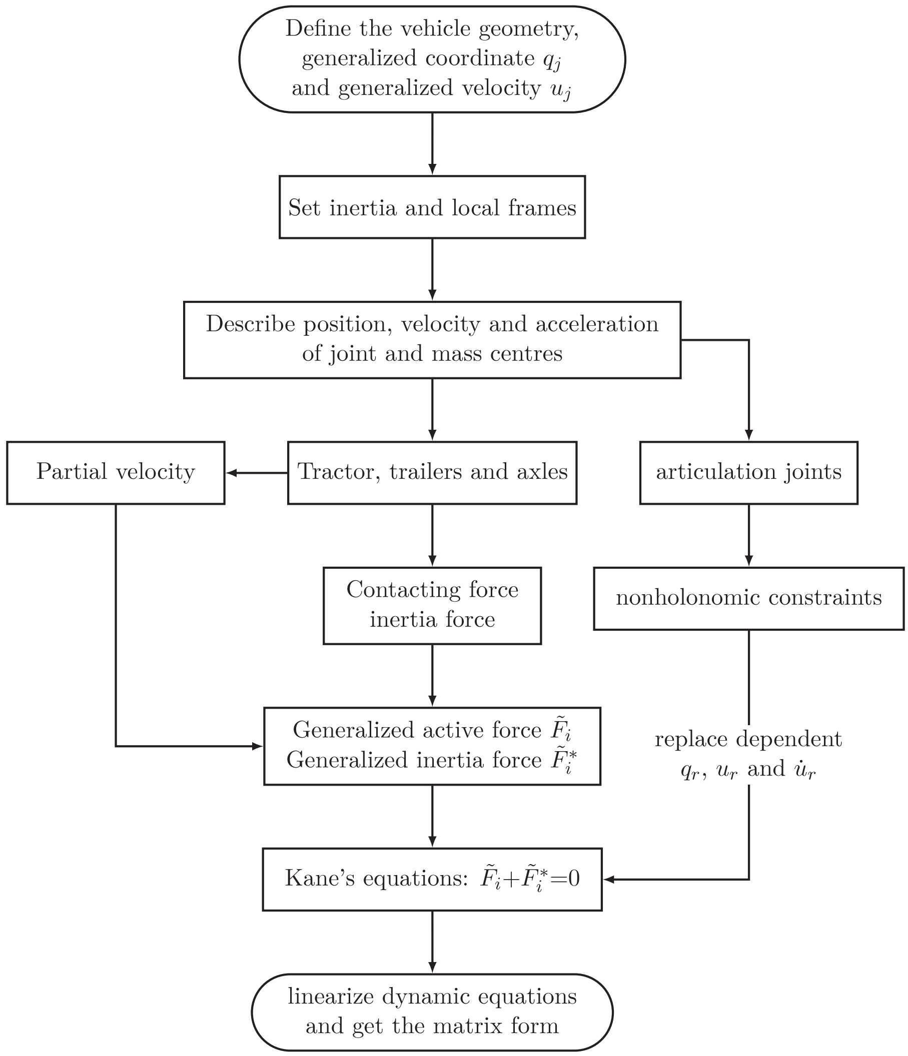

Fig. 1. The procedure for deriving the heavy vehicle dynamic model using Kane's method.

2.1. Development

The DOFs of the 9-axle B-Double are determined by the tractor and trailers' vertical displacements q_1, q_3, q_5, pitch rotations q_2, q_4, q_6, and vertical axle displacements $q_i, i = 7, \ldots, 15$. Therefore there are 15 generalized coordinates in the system, in total. Four reference frames including one inertial frame and three local frames are set for the vehicle system which are shown in Fig. 2(a): the Newtonian (inertial) frame N ($\mathbf{n_1}, \mathbf{n_2}, \mathbf{n_3}$), which has the origin fixed at the centre of gravity of the trailer C on the ground surface; Frame A ($\mathbf{a_1}, \mathbf{a_2}, \mathbf{a_3}$), where the origin is fixed at the centre of gravity of the tractor A; Frame B ($\mathbf{b_1}, \mathbf{b_2}, \mathbf{b_3}$), where the origin is fixed at the centre of gravity of the trailer B, and; Frame C ($\mathbf{c_1}, \mathbf{c_2}, \mathbf{c_3}$), where the origin is fixed at the centre of gravity of the trailer C. The angles between Frames N and A, N and B, and N and C are denoted as q_2, q_4 and q_6 respectively, and the transformation from frames N to A can be expressed by:

$$\begin{Bmatrix} \mathbf{n}_1 \\ \mathbf{n}_2 \\ \mathbf{n}_3 \end{Bmatrix} = \begin{bmatrix} \cos q_2 & \sin q_2 & 0 \\ -\sin q_2 & \cos q_2 & 0 \\ 0 & 0 & 1 \end{bmatrix} \begin{Bmatrix} \mathbf{a}_1 \\ \mathbf{a}_2 \\ \mathbf{a}_3 \end{Bmatrix}. \tag{2}$$

The transformation matrices from Frames N to B or C can be derived similarly by replacing q_2 to q_4 or to q_6. The tractor and two trailers are connected by two articulation (fifth wheel) constraints P_1 and P_2, where the positions of P_1 in frames A and B, and P_2 in frames B and C, with respect to Newtonian frame, are described as:

$$\mathbf{P}_1^A = (s_3 \cos q_6 - r_2 \cos q_4 + s_2 \cos q_2)\mathbf{n}_1 + (q_1 + \tau^A - r_1 \sin q_2)\mathbf{n}_2, \tag{3a}$$

$$\mathbf{P}_1^B = (s_3 \cos q_6 - r_2 \cos q_4 + s_2 \cos q_2)\mathbf{n}_1 + (q_3 + \tau^B - s_2 \sin q_4)\mathbf{n}_2, \tag{3b}$$

$$\mathbf{P}_2^B = (s_3 \cos q_6)\mathbf{n}_1 + (q_3 + \tau^B - r_2 \sin q_4)\mathbf{n}_2, \tag{3c}$$

$$\mathbf{P}_2^C = (s_3 \cos q_6)\mathbf{n}_1 + (q_5 + \tau^C - s_3 \sin q_6)\mathbf{n}_2, \tag{3d}$$

where the initial height from the ground to the centre of mass of tractor A and trailers B and C are $\tau^A = \tau^B = \tau^C$.

If we define the generalized velocity as:

$$u_j = \dot{q}_j, \qquad j = 1, 2, \ldots, 15, \tag{4}$$

then the velocities of points P_1 and P_2 with respect to tractor A, trailers B and C are:

$$\begin{aligned} {}^N v^{P^{A_1}} &= (-s_3 \sin q_6 u_6 + r_2 \sin q_4 u_4 - s_1 \sin q_2 u_2)\mathbf{n}_1 \\ &\quad + (u_1 - r_1 \cos q_2 u_2)\mathbf{n}_2, \end{aligned} \tag{5a}$$

$${}^N v^{P^{B_1}} = (-s_3 \sin q_6 u_6 + r_2 \sin q_4 u_4 - s_1 \sin q_2 u_2)\mathbf{n}_1,$$

$${}^N v^{P^{B_2}} = (-s_3 \sin q_6 u_6)\mathbf{n}_1 + (u_3 - r_2 \cos q_4 u_4)\mathbf{n}_2, \tag{5b}$$

$${}^N v^{P^{C_2}} = (-s_3 \sin q_6 u_6)\mathbf{n}_1 + (u_5 - s_3 \cos q_6 u_6)\mathbf{n}_2 \tag{5c}$$

$$+ (u_3 - s_2 \cos q_4 u_4)\mathbf{n}_2. \tag{5d}$$

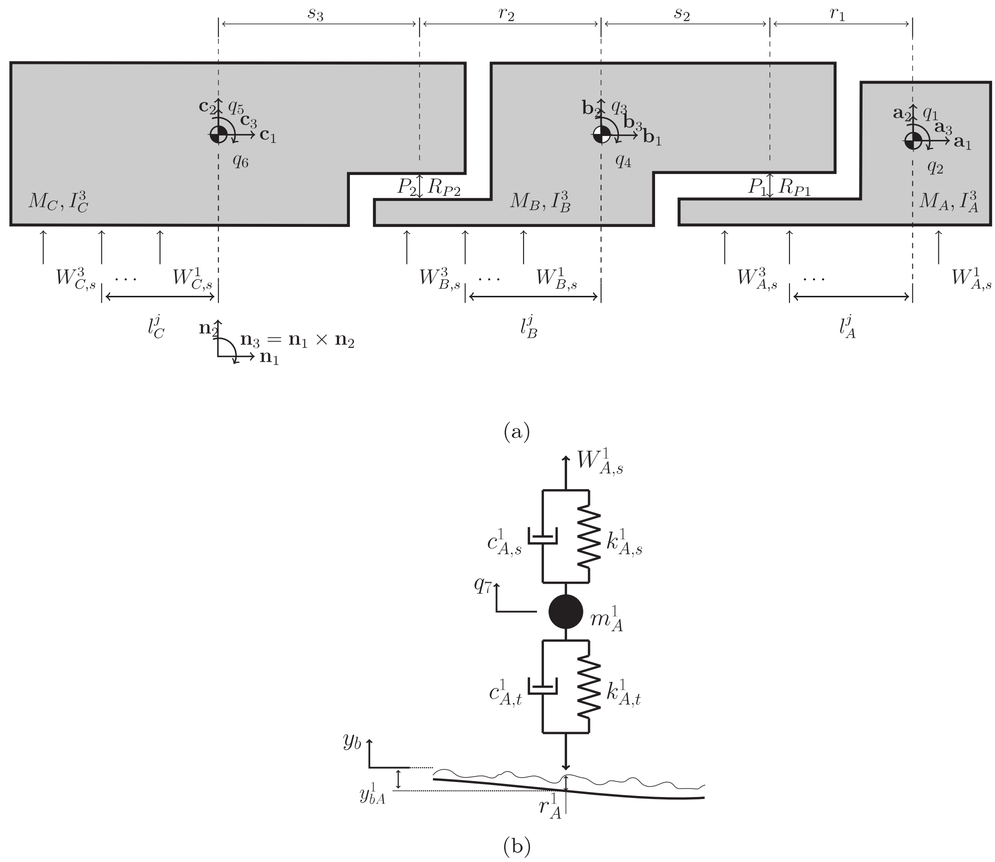

Fig. 2. Multi-body vehicle dynamic models: (a) Schematic diagram of B-double vehicle; (b) Suspension–axle–tyre system of the first axle of tractor.

Similarly, the accelerations of points P_1 and P_2 are obtained as:

$$\begin{aligned}{}^{N}a^{P^{A_1}} &= (-s_3 \sin q_6 \dot{u}_6 + r_2 \sin q_4 \dot{u}_4 - s_1 \sin q_2 \dot{u}_2 - s_3 \cos q_6 u_6^2 \\ &\quad + r_2 \cos q_4 u_4^2 - s_1 \cos q_2 u_2^2)\mathbf{n}_1 \\ &\quad + (\dot{u}_1 - r_1 \cos q_2 \dot{u}_2 + r_1 \sin q_2 u_2^2)\mathbf{n}_2,\end{aligned} \tag{6a}$$

$$\begin{aligned}{}^{N}a^{P^{B_1}} &= (-s_3 \sin q_6 \dot{u}_6 + r_2 \sin q_4 \dot{u}_4 - s_1 \sin q_2 \dot{u}_2 - s_3 \cos q_6 u_6^2 \\ &\quad + r_2 \cos q_4 u_4^2 - s_1 \cos q_2 u_2^2)\mathbf{n}_1,\end{aligned} \tag{6b}$$

$$\begin{aligned}{}^{N}a^{P^{B_2}} &= (-s_3 \sin q_6 \dot{u}_6 - s_3 \cos q_6 u_6^2)\mathbf{n}_1 \\ &\quad + (\dot{u}_3 - r_2 \cos q_4 \dot{u}_4 + r_2 \sin q_4 u_4^2)\mathbf{n}_2 \\ &\quad + (\dot{u}_3 - s_2 \cos q_4 \dot{u}_4 + s_2 \sin q_4 u_4^2)\mathbf{n}_2,\end{aligned} \tag{6c}$$

$$\begin{aligned}{}^{N}a^{P^{C_2}} &= (-s_3 \sin q_6 \dot{u}_6 - s_3 \cos q_6 u_6^2)\mathbf{n}_1 \\ &\quad + (\dot{u}_5 - s_3 \cos q_6 \dot{u}_6 + s_3 \sin q_6 u_6^2)\mathbf{n}_2.\end{aligned} \tag{6d}$$

Supposing that there is no slippage at the articulation points (fifth wheels), then the position, velocity, and acceleration of the articulation points in each local frame with respect to the N frame are equivalent. Therefore the nonholonomic constraint equations can be obtained from Eqs. (3), (5) and (6) as:

$$q_3 = q_1 - r_1 \sin q_2 + s_2 \sin q_4, \tag{7a}$$

$$q_5 = q_1 - r_1 \sin q_2 + (s_2 - r_2) \sin q_4 + s_3 \sin q_6, \tag{7b}$$

$$u_3 = u_1 - r_1 \cos q_2 u_2 + s_2 \cos q_4 u_4, \tag{7c}$$

$$u_5 = u_1 - r_1 \cos q_2 u_2 + (s_2 - r_2) \cos q_4 u_4 + s_3 \cos q_6 u_6, \tag{7d}$$

$$\dot{u}_3 = \dot{u}_1 - r_1 \cos q_2 \dot{u}_2 + s_2 \cos q_4 \dot{u}_4 + r_1 \sin q_2 u_2^2 - s_2 \sin q_4 u_4^2, \tag{7e}$$

$$\begin{aligned}\dot{u}_5 &= \dot{u}_1 - r_1 \cos q_2 \dot{u}_2 + (s_2 - r_2) \cos q_4 \dot{u}_4 + s_3 \cos q_6 \dot{u}_6 \\ &\quad + r_1 \sin q_2 u_2^2 - (s_2 - r_2) \sin q_4 u_4^2 - s_3 \sin q_6 u_6^2.\end{aligned} \tag{7f}$$

In this case, vertical displacements of trailers B and C (q_3 and q_5) are selected as the dependent generalized coordinates.

2.2. Generalized rates

The angular and linear velocities and accelerations of tractor A with respect to the Newtonian (N) frame are given by:

$${}^{N}\omega^{A} = -u_2 \mathbf{n_3}, \tag{8a}$$

$${}^{N}\alpha^{A} = -\dot{u}_2 \mathbf{n_3}, \tag{8b}$$

$${}^{N}v^{A^*} = u_1 \mathbf{n_2}, \tag{8c}$$

$${}^{N}a^{A^*} = \dot{u}_1 \mathbf{n_2}. \tag{8d}$$

In the same way, the angular and linear velocities and accelerations of trailer B with respect to N are:

$${}^{N}\omega^{B} = -u_4 \mathbf{n_3}, \tag{9a}$$

$${}^{N}\alpha^{B} = -\dot{u}_4 \mathbf{n_3}, \tag{9b}$$

$${}^{N}v^{B^*} = u_3 \mathbf{n_2}, \tag{9c}$$

$${}^{N}a^{B^*} = \dot{u}_3 \mathbf{n_2}, \tag{9d}$$

where u_3 and $\dot{u}_3$ are given in Eqs. (7c) and (7e), and the angular and linear velocities and accelerations of trailer C with respect to N are:

$${}^{N}\omega^{C} = -u_6 \mathbf{n_3}, \tag{10a}$$

$${}^{N}\alpha^{C} = -\dot{u}_6 \mathbf{n_3}, \tag{10b}$$

$${}^{N}v^{C^*} = u_5 \mathbf{n_2}, \tag{10c}$$

$${}^{N}a^{C^*} = \dot{u}_5 \mathbf{n_2}, \tag{10d}$$

where u_5 and $\dot{u}_5$ are given in Eqs. (7d) and (7f). Finally, the velocities and accelerations of the axles on the tractor and trailers are, for $j = 1, 2, 3$, given by:

$$^N v^{(Aj)} = u_{6+j}\mathbf{n}_2, \tag{11a}$$

$$^N v^{Bj} = u_{9+j}\mathbf{n}_2, \tag{11b}$$

$$^N v^{Cj} = u_{12+j}\mathbf{n}_2, \tag{11c}$$

$$^N a^{Aj} = \dot{u}_{6+j}\mathbf{n}_2, \tag{11d}$$

$$^N a^{Bj} = \dot{u}_{9+j}\mathbf{n}_2, \tag{11e}$$

$$^N a^{Cj} = \dot{u}_{12+j}\mathbf{n}_2. \tag{11f}$$

2.3. Contact and inertial forces

The constraint force between tractor A and trailer B at point P_1 and that between trailers B and C are denoted as $R_{P1}\mathbf{n}_1$ and $R_{P2}\mathbf{n}_1$ respectively. Thus, the external forces and torques acting on the centre of mass of tractor A are:

$$\mathbf{R}_A = \left(\sum_{j=1}^{3} W_{A,s}^j + R_{P1}\right)\mathbf{n}_2, \tag{12a}$$

$$\mathbf{T}_A = \left(\cos q_2 \sum_{j=1}^{3} W_{A,s}^j L_A^j + R_{P1} r_1 \cos q_2\right)\mathbf{n}_3, \tag{12b}$$

in which,

$$W_{A,s}^j = k_{A,s}^j\left[q_{6+j} - q_1 + L_A^j \sin q_2\right] + c_{A,s}^j\left[\dot{q}_{6+j} - \dot{q}_1 + L_A^j \sin \dot{q}_2\right].$$

Similarly, the external forces and torques acting on trailers B and C are:

$$\mathbf{R}_B = \left(\sum_{j=1}^{3} W_{B,s}^j - R_{P1} + R_{P2}\right)\mathbf{n}_2, \tag{13a}$$

$$\mathbf{T}_B = \left(\cos q_4 \sum_{j=1}^{3} W_{B,s}^j L_B^j - R_{P1} s_2 \cos q_4 + R_{P2} r_2 \cos q_4\right)\mathbf{n}_3, \tag{13b}$$

and

$$\mathbf{R}_C = \left(\sum_{j=1}^{3} W_{C,s}^j - R_{P2}\right)\mathbf{n}_2, \tag{14a}$$

$$\mathbf{T}_C = \left(\cos q_6 \sum_{j=1}^{3} W_{C,s}^j L_C^j - R_{P2} s_3 \cos q_6\right)\mathbf{n}_3, \tag{14b}$$

in which,

$$W_{B,s}^j = k_{B,s}^j\left[q_{9+j} - q_3 + L_B^j \sin q_4\right] + c_{B,s}^j\left[\dot{q}_{9+j} - \dot{q}_3 + L_B^j \sin \dot{q}_4\right],$$

and

$$W_{C,s}^j = k_{C,s}^j\left[q_{12+j} - q_5 + L_C^j \sin q_6\right] + c_{C,s}^j\left[\dot{q}_{12+j} - \dot{q}_5 + L_C^j \sin \dot{q}_6\right].$$

The contact forces acting on the axles for the tractor and trailers are:

$$\mathbf{R}_{Aj} = \left(-W_{A,s}^j - k_{A,t}^j q_{6+j}\mathbf{n}_2\right), \tag{15a}$$

$$\mathbf{R}_{Bj} = \left(-W_{B,s}^j - k_{B,t}^j q_{9+j}\mathbf{n}_2\right), \tag{15b}$$

$$\mathbf{R}_{Cj} = \left(-W_{C,s}^j - k_{C,t}^j q_{12+j}\mathbf{n}_2\right). \tag{15c}$$

The inertial torques are:

$$\mathbf{T}^* = -\alpha \cdot \mathbf{I} - \omega \times \mathbf{I} \cdot \omega, \tag{16}$$

where $\mathbf{I}$ is the central inertial dyadic, and α and ω are the angular accelerations and velocities respectively. Substitute Eq. (8) into Eq. (16), and transform the local coordinates frame to N frame by Eq. (2) to find:

$$\begin{aligned}\mathbf{T}_A^* &= \dot{u}_2\mathbf{n_3} \cdot (I_A^1\mathbf{a_1a_1} + I_A^2\mathbf{a_2a_2} + I_A^3\mathbf{a_3a_3}) \\ &\quad - u_2\mathbf{n_3} \times (I_A^1\mathbf{a_1a_1} + I_A^2\mathbf{a_2a_2} + I_A^3\mathbf{a_3a_3}) \cdot u_2\mathbf{n_3} \\ &= \dot{u}_2 I_A^3\mathbf{n_3}.\end{aligned} \tag{17}$$

Similarly, the inertial torque of trailers B and C can be obtained by substituting Eqs. (9) and (10) into Eq. (16) to get:

$$\mathbf{T}_B^* = \dot{\mathbf{u}}_4 I_B^3\mathbf{n_3}, \tag{18a}$$

$$\mathbf{T}_C^* = \dot{\mathbf{u}}_6 I_C^3\mathbf{n_3}. \tag{18b}$$

2.4. Generalized active and inertial forces

The generalized active forces of the nonholonomic system can be expressed generally as:

$$\begin{aligned}\tilde{F}_i &= {}^N\tilde{\omega}_i^A \cdot \mathbf{T}_A + {}^N\tilde{v}_i^{A^*} \cdot \mathbf{R}_A + {}^N\tilde{\omega}_i^B \cdot \mathbf{T}_B + {}^N\tilde{v}_i^{B^*} \cdot \mathbf{R}_B + {}^N\tilde{v}_i^{C^*} \cdot \mathbf{R}_C \\ &\quad + \sum_{j=1}^{3} {}^N v_i^{Aj} \cdot \mathbf{R}_{Aj} + \sum_{j=1}^{3} {}^N v_i^{Bj} \cdot \mathbf{R}_{Bj} + \sum_{j=1}^{3} {}^N v_i^{Cj} \cdot \mathbf{R}_{Cj},\end{aligned} \tag{19}$$

where $i = 1, \ldots, 15$ but $i \neq 3, 5$, which are the dependent coordinates, Eq. (7). In Eq. (19) the contact forces $\mathbf{R}$ and torque $\mathbf{T}$ can be obtained from Eqs. (12) to (15); the ith partial velocity $\tilde{v}_i$ and partial angular velocity $\tilde{\omega}_i$ are the coefficients for u_i and can be obtained from Eqs. (8) tp (11). The generalized active forces of tractor and trailers then become:

$$\begin{aligned}\tilde{F}_1 &= \mathbf{R}_A\mathbf{n}_2 + \mathbf{R}_B\mathbf{n}_2 + \mathbf{R}_C\mathbf{n}_2 \\ &= \sum_{j=1}^{3} W_{A,s}^j + \sum_{j=1}^{3} W_{B,s}^j + \sum_{j=1}^{3} W_{C,s}^j,\end{aligned} \tag{20a}$$

$$\begin{aligned}\tilde{F}_2 &= -\mathbf{n}_3 \cdot \mathbf{T}_A - r_1 \cos q_2\, \mathbf{n}_2 \cdot \mathbf{R}_B - r_1 \cos q_2\, \mathbf{n}_2 \cdot \mathbf{R}_C \\ &= -\cos q_2 \sum_{j=1}^{3} W_{A,s}^j L_A^j - r_1 \cos q_2 \left(\sum_{j=1}^{3} W_{B,s}^j + \sum_{j=1}^{3} W_{C,s}^j\right),\end{aligned} \tag{20b}$$

$$\begin{aligned}\tilde{F}_4 &= -\mathbf{n}_3 \cdot \mathbf{T}_B + s_2 \cos q_4\, \mathbf{n}_2 \cdot \mathbf{R}_B + \left(s_2 - r_2\right) \cos q_4\, \mathbf{n}_2 \cdot \mathbf{R}_C \\ &= -\cos q_4 \sum_{j=1}^{3} W_{B,s}^j L_B^j + s_2 \cos q_4 \sum_{j=1}^{3} W_{B,s}^j \\ &\quad + (s_2 - r_2) \sum_{j=1}^{3} W_{C,s}^j,\end{aligned} \tag{20c}$$

$$\begin{aligned}\tilde{F}_6 &= -\mathbf{n}_3 \cdot \mathbf{T}_C + s_3 \cos q_6\, \mathbf{n}_2 \cdot \mathbf{R}_C \\ &= -\cos q_6 \sum_{j=1}^{3} W_{C,s}^j L_C^j + s_3 \cos q_6 \sum_{j=1}^{3} W_{C,s}^j.\end{aligned} \tag{20d}$$

The generalized active forces of axles are derived for $j = 1, 2, 3$, as follows:

$$\tilde{F}_{6+j} = \mathbf{n}_2 \cdot \mathbf{R}_{Aj} = -W_{A,s}^j - k_{A,t}^j q_{9+j}, \tag{21a}$$

$$\tilde{F}_{9+j} = \mathbf{n}_2 \cdot \mathbf{R}_{Bj} = -W_{B,s}^j - k_{B,t}^j q_{12+j}, \tag{21b}$$

$$\tilde{F}_{12+j} = \mathbf{n}_2 \cdot \mathbf{R}_{Cj} = -W_{C,s}^j - k_{C,t}^j q_{15+j}. \tag{21c}$$

The generalized inertial forces can be expressed as:

$$\begin{aligned}\tilde{F}_i^* &= {}^N\tilde{\omega}_i^A \cdot \mathbf{T}_A^* - M_A {}^N a^{A^*} \cdot {}^N\tilde{v}_i^{A^*} + {}^N\tilde{\omega}_i^B \cdot \mathbf{T}_B^* - M_B {}^N a^{B^*} \cdot {}^N\tilde{v}_i^{B^*} \\ &\quad + {}^N\tilde{\omega}_r^C \cdot \mathbf{T}_C^* - M_C {}^N a^{C^*} \cdot {}^N\tilde{v}_i^{C^*} - \sum_{j=1}^{3} m_A^j {}^N a^{A_j^*} \cdot {}^N\tilde{v}_i^{A_j} \\ &\quad - \sum_{j=1}^{3} m_B^j {}^N a^{B_j^*} \cdot {}^N\tilde{v}_i^{B_j} - \sum_{j=1}^{3} m_C^j {}^N a^{C_j^*} \cdot {}^N\tilde{v}_i^{C_j},\end{aligned} \tag{22}$$

where $i = 1, \ldots, 15$ but as before $i \neq 3, 5$, which are the dependent coordinates, Eq. (7).

The inertial torque $\mathbf{T}^*$ is introduced from Eqs. (17) to (18), where a^* is the acceleration of rigid body or particle. The generalized inertial forces of the tractor and trailers are then obtained as:

$$\begin{aligned}\tilde{F}_1^* &= -M_A {}^N a^{A^*} \cdot\ \mathbf{n}_2 - M_B {}^N a^{B^*} \cdot\ \mathbf{n}_2 - M_C {}^N a^{C^*} \cdot\ \mathbf{n}_2 \\ &= -(M_A + M_B + M_C)\dot{u}_1 + (r_1 \cos q_2\, M_B + r_1 \cos q_2\, M_C)\dot{u}_2\end{aligned}$$

$$-\left[s_2\cos q_4\,M_B+(s_2-r_2)\cos q_4\,M_C\right]\dot{u}_4-\left(s_3\cos q_6\,M_C\right)\dot{u}_8 -\left(r_1\sin q_2\,M_B+r_1\sin q_2\,M_C\right)u_2^2 +\left[s_2\sin q_4\,M_B+(s_2-r_2)\sin q_4\,M_C\right]u_4^2+(s_3\sin q_6\,M_C)u_6^2, \tag{23a}$$

$$\begin{aligned}\tilde{F}_2^*&=-\mathbf{n}_3\cdot\mathbf{T}_A^*+M_B{}^Na^{B^*}r_1\cos q_2\mathbf{n}_2+M_C{}^Na^{C^*}r_1\cos q_2\mathbf{n}_2\\&=(r_1\cos q_2\,M_B+r_1\cos q_2\,M_C)\dot{u}_1\\&\quad-(I_A^3+r_1^2\cos^2 q_2\,M_B+r_1^2\cos^2 q_2\,M_C)\dot{u}_2\\&\quad+\cos q_2\,\cos q_4\cdot\left[r_1s_2M_B+r_1(s_2-r_2)M_C\right]\dot{u}_4\\&\quad+\cos q_2\,\cos q_6\cdot r_1s_3M_C\dot{u}_6\\&\quad+\left(M_B+M_C\right)r_1^2\cos q_2\,\sin q_2\,u_2^2\\&\quad-\cos q_2\,\sin q_4\cdot\left[r_1s_2M_B+r_1(s_2-r_2)M_C\right]u_4^2\\&\quad-\cos q_2\,\sin q_6\cdot r_1s_3M_Cu_6^2,\end{aligned}\tag{23b}$$

$$\begin{aligned}\tilde{F}_4^*&=-\mathbf{n}_3\cdot\mathbf{T}_B^*-M_B{}^Na^{B^*}s_2\cos q_4\mathbf{n}_2-M_C{}^Na^{C^*}(s_2-r_2)\cos q_4\mathbf{n}_2\\&=-[s_2\cos q_4M_B+(s_2-r_2)\cos q_4M_C]\dot{u}_1\\&\quad+\cos q_2\cos q_5\cdot[r_1s_2M_B+r_1(s_2-r_2)M_C]\dot{u}_2\\&\quad-\cos^2 q_4[I_B^3+s_2^2M_B+(s_2-r_2)^2M_C]\dot{u}_4\\&\quad-\cos q_4\cos q_6\cdot s_3(s_2-r_2)M_C\dot{u}_8\\&\quad+\sin q_2\cos q_4\cdot[r_1s_2M_B+r_1(s_2-r_2)M_C]u_2^2\\&\quad+\sin q_6\cos q_4\cdot s_3(s_2-r_2)M_Cu_6^2,\end{aligned}\tag{23c}$$

$$\begin{aligned}\tilde{F}_6^*&=-\mathbf{n}_3\cdot\mathbf{T}_C^*-M_C{}^Na^{C^*}s_3\cos q_6\,\mathbf{n}_2\\&=-(s_3\cos q_6\,M_C)\dot{u}_1+\left[\cos q_2\,\cos q_6\,r_1s_3M_C\right]\dot{u}_2\\&\quad-\cos q_4\,\cos q_6\cdot s_3(s_2-r_2)M_C\dot{u}_4-\left[I_C^3+\cos^2 q_6\,s_3^2M_C\right]\dot{u}_6\\&\quad+\sin q_2\,\cos q_6\cdot r_1s_3M_Cu_2^2-\sin q_4\,\cos q_6\cdot s_3(s_2-r_2)M_Cu_4^2\\&\quad-\sin q_6\,\cos q_6\cdot s_3M_Cu_6^2.\end{aligned}\tag{23d}$$

And finally, the following set of generalized inertial forces for the axles are derived for $j=1,2,3$ as:

$$\tilde{F}_{6+j}^*=-m_{Aj}{}^Na^{A_j^*}\mathbf{n}_2=-m_{Aj}\dot{u}_{6+j}, \tag{24a}$$

$$\tilde{F}_{9+j}^*=-m_{Bj}{}^Na^{B_j^*}\mathbf{n}_2=-m_{Bj}\dot{u}_{9+j}, \tag{24b}$$

$$\tilde{F}_{12+j}^*=-m_{Cj}{}^Na^{C_j^*}\mathbf{n}_2=-m_{Cj}\dot{u}_{12+j}. \tag{24c}$$

2.5. Dynamic equations

Considering the dependent coordinates, Kane's dynamic equation is expressed as:

$$\tilde{F}_i+\tilde{F}_i^*=0,\qquad i=1,\dots,15;i\neq 3,5, \tag{25}$$

By substituting Eqs. (20), (21), (23) and (24) into Eq. (25), thirteen second-order differential equations for the B-Double vehicle are derived. Note that the vertical displacements q_3 and q_5 and velocities $u_3=\dot{q}_3$ and $u_5=\dot{q}_5$ of the trailers in the generalized active forces can be replaced by other independent generalized rates through the constraints Eq. (7). It can be seen that the interaction forces at hinges P_{12} and P_{22} are eliminated automatically by calculating the generalized active forces in Eq. (19) via Kane's method. In comparison, the interaction forces need to be derived explicitly in terms of a function of other forces in Newton–Euler method. Compared to previous methods, the equations of motion of the vehicle can be systematically and numerically derived, even though the non-linearity of the dynamic is taken into account.

By truncating the higher order terms and assuming small rotations (i.e. $\sin q=q$ and $\cos q=1$), the linearized second-order differential equations can be expressed in matrix form as:

$$\left[\mathbf{M}_v\right]\left\{\ddot{\mathbf{q}}\right\}+\left[\mathbf{C}_v\right]\left\{\dot{\mathbf{q}}\right\}+\left[\mathbf{K}_v\right]\left\{\mathbf{q}\right\}=\left\{\mathbf{F}_v\right\}, \tag{26}$$

where the mass, stiffness and damping matrices are expressed in Appendix A. The DOFs are defined by the generalized coordinates as:

$$\mathbf{q}=\begin{bmatrix}q_1 & q_2 & q_4 & q_6 & q_7 & q_8 & q_9 & \cdots & q_{15}\end{bmatrix}^T, \tag{27}$$

Table 1
Mechanical properties of the tractors and trailers.

		Unit	B-double	SA6	SA5
Tractor A	r_1	m	−2.427	−3.000	−2.600
	s_1	m	–	–	–
	M_A	kg	6550	6420	4891
	I_A^3	kg m^2	6604	6955	5955
	L_A^1	m	1.523	1.000	1.000
	L_A^2	m	−1.727	−2.300	−2.600
	L_A^3	m	−3.127	−3.700	–
	drive axle loads	kg	5664	6130	3846
	steering axle loads	kg	7714	6715	8266
Trailer B	r_2	m	−2.931	–	–
	s_2	m	5.369	5	5
	M_B	kg	18397	25374	19759
	I_B^3	kg m^2	10488	44933	34990
	L_B^1	m	−1.531	−2.700	−2.000
	L_B^2	m	−2.931	−4.100	−3.400
	L_B^3	m	−4.331	−5.500	−4.800
	trailer axle loads	kg	6479	5580	5511
Trailer C	r_3	m	–	–	–
	s_3	m	5.895	–	–
	M_C	kg	27375	–	–
	I_C^3	kg m^2	15488	–	–
	L_C^1	m	−1.705	–	–
	L_C^2	m	−3.105	–	–
	L_C^3	m	−4.505	–	–
	trailer axle loads	kg	6397	–	–

and the force vector is given by:

$$\mathbf{F}_v=\left[\mathbf{0}_{(4\times1)}\quad f_1\quad f_2\cdots\quad f_9\right]^T, \tag{28}$$

where f_i is the contact force caused by the road roughness r_i and bridge displacement y_{bi} at the ith wheel of vehicle, which is defined by:

$$f_i=k_t^i\left(r_i+y_{bi}\right)+c_t^i\left(\dot{r}_i+\dot{y}_{bi}\right), \tag{29}$$

where k_t^i and c_t^i are the ith tyre stiffness and damping.

2.6. Vehicle parameters

The parameters of B-double vehicle used in this study are taken here to be in conformance with the Heavy Vehicle National Law provided by Heavy Vehicle National Regulator (NHVR) in Australia [23,32,33]. In addition, two types of semi-trailers are introduced as comparison: the 5-axle single articulated truck (SA5) and the 6-axle single articulated truck (SA6) studied previously, [9]. The linear vehicle models of SA5 and SA6 derived by Kane's method are identical to that of in [9,34]. The parameters of tractors and trailers of three vehicles are presented in Table 1, while the mechanical vehicle properties of axles for three vehicles types are the same and shown in Table 2.

3. Bridge model

3.1. General development

The simply supported Euler–Bernoulli beam of length L_b is assumed to represent the bridge model. The governing equation for the beam is:

$$\rho\frac{\partial^2 y_b(x,t)}{\partial t^2}+\mu\frac{\partial y_b(x,t)}{\partial t}+EI\frac{\partial^4 y_b(x,t)}{\partial x^4}=p(x,t), \tag{30}$$

where ρ is the mass per unit length; μ is the damping per unit length; E is the elastic modulus; I is the second moment of area; $y_b(x,t)$ is the displacement of beam on point x at time t, and; $p(x,t)$ is the force on point x at time t. By using modal superposition the vertical displacement of beam can be expressed by a set of n vibration modes:

$$y_b(x,t)=\sum_{i=1}^{n}\phi_i(x)\,\eta_i(t), \tag{31}$$

Table 2
Mechanical properties of the axles.

Suspension stiffness	kN m^{-1}
drive axles	1000
steering axles	400
trailer axles	1000
Suspension damping	**kN s m^{-1}**
drive axles	20
steering axles	10
trailer axles	20
Tyre stiffness	**kN m^{-1}**
drive axles	3500
steering axles	1750
trailer axles	3500
Axle mass	**kg**
drive axles	1100
steering axles	700
trailer axles	750

where $\phi_i(x)$ are the vibration mode shapes and $\eta_i(t)$ are the modal coordinates. The jth mode shape at position x can be rewritten as:

$$\phi_j(x) = \sqrt{\frac{2}{\rho L_b}} \sin\left(\frac{j\pi x}{L_b}\right). \tag{32}$$

Considering the force as a point load, the force caused by a 9-axle vehicle can be expressed as:

$$p(x,t) = \sum_{i=1}^{9} F_b(x_i,t)\,\phi_j(x_i)\,I(x_i), \tag{33}$$

in which x_i is the position of the ith tyre. When the tyre is on the beam the indicator function $I(x_i)$ is 1, otherwise it is 0. The dynamic interaction force F_b for wheel i can be expressed as:

$$F_b(x_i,t) = W_i - f_i(x_i,t), \tag{34}$$

in which W_i is the static wheel force, and $f_i(x_i,t)$ is the dynamic contact force. With this arrangement, the jth mode equation of motion for the bridge can be expressed in the simple form:

$$\ddot{\eta}_j + 2\xi_j\omega_j\dot{\eta}_j + \omega_j^2\eta_j = \sum_{i=1}^{9}\left[W_i - f_i(x_i,t)\right]\phi_j(x_i)\,I(x_i). \tag{35}$$

3.2. Consideration of hog

According to the design code AS 5100.5 [17], at long-term, an upward hog is required for deflection serviceability, and this is a common situation in practice for many bridges. For this work, the hog is taken to have a sinusoidal curve, which has the same format of the first mode shape, although any profile can be taken. The hog height at mid-span is denoted as h_0 as shown in Fig. 3(a), and so the deflected profile of the bridge without external loading is:

$$r_h(x) = h_0 \sin\left(\frac{\pi x}{L_b}\right). \tag{36}$$

For the VBI problem, consideration of the hog can be done similar to the road roughness profile, which contributes to dynamic contact force $f_i(x_i,t)$. Then the corresponding road roughness, $r(x_i)$, in Eq. (29) can be expressed as the sum of pavement variation and hog:

$$r(x) = r_p(x) + r_h(x). \tag{37}$$

3.3. Single vehicle on a single span bridge

The complete VBI system equations are formed by the equations of motion of the vehicle(s) and bridge, coupled by the dynamic interaction forces at the contact points between the tyres and bridge surface. The coupled VBI system for a single vehicle on a single bridge is:

$$[\mathbf{M_c}]\{\ddot{\mathbf{q}}_c\} + [\mathbf{C_c}]\{\dot{\mathbf{q}}_c\} + [\mathbf{K_c}]\{\mathbf{q}_c\} = \{\mathbf{F}_c\}, \tag{38}$$

where $\mathbf{F}_c$ is the coupled force vector, $\mathbf{M_c}$ is the coupled mass matrix, and $\mathbf{K_c}$ and $\mathbf{C_c}$ are the coupled stiffness and damping matrices, which vary with time. The displacement vector $\mathbf{q_c} = (\mathbf{q},\boldsymbol{\eta})^T$ consists of the displacement of the vehicle and the modal coordinates of bridge. These matrices and vectors can be found in Appendix C.

3.4. Single vehicle on a discontinuous multi-span bridge

The multi-span discontinuous bridge is taken to be composed of multiple simply-supported beams. When the vehicle is moving on a N-spans viaduct, the coupled equation of motion is given by:

$$[\mathbf{M_{cN}}]\{\ddot{\mathbf{q}}_{cN}\} + [\mathbf{C_{cN}}]\{\dot{\mathbf{q}}_{cN}\} + [\mathbf{K_{cN}}]\{\mathbf{q}_{cN}\} = \{\mathbf{F}_{cN}\}, \tag{39}$$

in which,

$$\mathbf{M_{cN}} = \begin{bmatrix} \mathbf{M}_v & 0 & \cdots & 0 \\ 0 & \mathbf{M}_{b1} & \cdots & 0 \\ \vdots & \vdots & \ddots & \vdots \\ 0 & 0 & \cdots & \mathbf{M}_{bN} \end{bmatrix}, \tag{40}$$

$$\mathbf{C_c} = \begin{bmatrix} \mathbf{C}_v & \mathbf{C}_{vb1} & \mathbf{C}_{vb2} & \cdots & \mathbf{C}_{vbN} \\ \mathbf{C}_{b1v} & \mathbf{C}_{b1} + \mathbf{C}_{b1b1} & 0 & \cdots & 0 \\ \mathbf{C}_{b2v} & 0 & \mathbf{C}_{b2} + \mathbf{C}_{b2b2} & \cdots & 0 \\ \vdots & \vdots & \vdots & \ddots & \vdots \\ \mathbf{C}_{bNv} & 0 & 0 & \cdots & \mathbf{C}_{bN} + \mathbf{C}_{bNbN} \end{bmatrix}, \tag{41}$$

$$\mathbf{K_c} = \begin{bmatrix} \mathbf{K}_v & \mathbf{K}_{vb1} & \mathbf{K}_{vb2} & \cdots & \mathbf{K}_{vbN} \\ \mathbf{K}_{b1v} & \mathbf{K}_{b1} + \mathbf{K}_{b1b1} & 0 & \cdots & 0 \\ \mathbf{K}_{b2v} & 0 & \mathbf{K}_{b2} + \mathbf{K}_{b2b2} & \cdots & 0 \\ \vdots & \vdots & \vdots & \ddots & \vdots \\ \mathbf{K}_{bNv} & 0 & 0 & \cdots & \mathbf{K}_{bN} + \mathbf{K}_{bNbN} \end{bmatrix}, \tag{42}$$

and

$$\{\mathbf{F}_c\} = \begin{Bmatrix} \mathbf{0}_{(4\times1)} \\ \mathbf{F}_v \\ [\mathbf{N}_{b1}]\{\mathbf{F_{b1}}\} \\ \vdots \\ [\mathbf{N}_{bN}]\{\mathbf{F_{bN}}\} \end{Bmatrix}. \tag{43}$$

where the mass matrix $\mathbf{M}_b$, stiffness matrix $\mathbf{K}_b$, damping matrix $\mathbf{C}_b$, mode shape matrix $\mathbf{N}_b$, and force vector $\mathbf{F}_b$ are given in Appendix B. The time-dependent matrices and vectors can be obtained in Section 3.3, where the jth mode shape matrix $\mathbf{N}_{bj}$ turns zero once the vehicle is not in contact with the jth span of the viaduct. The coupled VBI system can be solved by any step-by-step integration method and the Newmark–Beta algorithm is applied in this study.

3.5. Validation

Fig. 4 shows a validation of the VBI model by comparing the dynamic bending moment and acceleration at the mid-span with [9], where the same bridge and vehicle properties are selected. It shows that the bridge model derived by the modal superposition method has a good match with the finite element model used [9]. Small discrepancies are likely because the pitch moment of inertia and centre of gravity are not provided in [9] and were estimated. The first ten modes are considered for superposition model which makes strong agreement with finite element model when all the parameters are same.

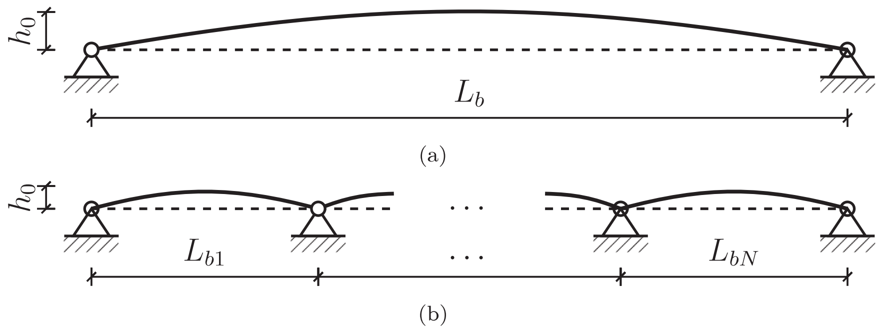

Fig. 3. Consideration of hog: (a) Simply supported bridge; (b) Discontinuous multi-span viaduct.

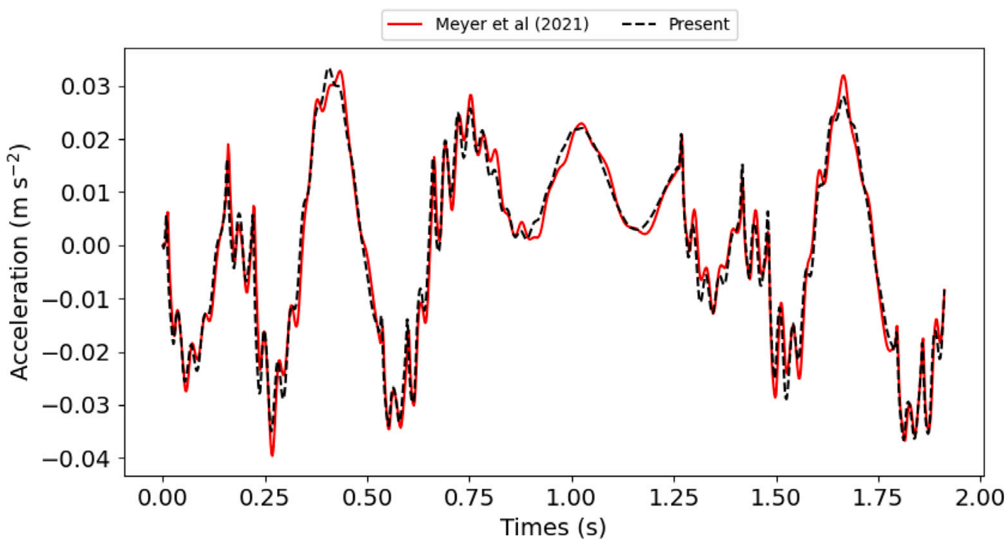

Fig. 4. Mid-span acceleration for SA6 vehicle crossing 28 m bridge at speed 80 km h^{-1} from the present model and [9].

4. Influence of bridge hog

To investigate the influence of hog of PSC girder-type bridges on VBI, the bridge is taken as a simply-supported beam, as is typical for this structural form. As noted above, the hog is treated with the road profile and so does not change any structural properties. The hog height, h_0, considered ranges from 0 to $L_b/400$. The interaction between the simply-supported bridge and the three vehicles considered are compared to understand the effect of the hog on the DAF. We consider first the link between DAF, vehicle speed and hog, for a fixed span length. Then, we consider, for a fixed vehicle speed, the influence of span length and hog on DAF.

Further to the general definition of Eq. (1), the specific DAF taken here, following [34], is:

$$\mathrm{DAF} = \frac{M_T}{M_S}, \tag{44}$$

where the total bending moment (M_T) is the sum of the static and dynamic bending moments, $M_T = M_S + M_D$.

4.1. Vehicle velocity and bridge hog

The simply-supported bridge used has length L_b = 28 m, mass per unit length ρ = 19 929 kg/m, and flexural rigidity EI = 6.6 × 10^{10} Nm^2. The hog height h_0 ranges from 0 to 70 mm ($L_b/400$) in 1 mm intervals, and the vehicle travels at a range of speeds from 20 km h^{-1} to 140 km h^{-1} in 1 km h^{-1} intervals. The vehicle parameters are as shown in Table 1, and the three types of vehicle have the same axle properties, as shown in Table 2. Both a smooth profile and a Class B road profile [35], randomly generated for each hog and speed, are used for comparison.

4.1.1. Results

Fig. 5(a) shows the hog has less influence on the B-Double vehicle system if the vehicle speed is lower than 60 km h^{-1}. When the B-double travels faster than 60 km h^{-1}, two critical speeds are observed at around 74 km h^{-1} and 116 km h^{-1} where a significant increase of amplification around the resonance speed due to hogging is obtained. It can be seen from Fig. 5(c) that the hog amplifies the DAF caused by SA6 when the speed is over about 64 km h^{-1}, and a significant increase is observed at high velocities nearing 140 km h^{-1}. However, the hog slightly reduces the DAF at a low resonant speed around 52 km h^{-1}. Increasing hog slightly increases the DAF when SA5 crosses the bridge at higher speeds from 120 km h^{-1} to 140 km h^{-1} and at the resonant speed around 57 km h^{-1} as shown in Fig. 5(e). Interestingly, the DAF reduces notably with the increase of hog height at the resonant speed around 99 km h^{-1} and anti-resonant speed around 77 km h^{-1}. As road roughness Class B is taken into account, Figs. 5(b), 5(d) and 5(f) show that the increased and reduced DAF caused by the hog is still observed at the respective speed ranges.

4.1.2. Discussion

For the vehicles with 3-axle tractors like the B-double and SA6, the hog is more likely to cause an increased DAF for most of the velocity range. In contrast, hog has less influence on the SA5 truck which has a 2-axle tractor, and it even reduces the amplification at mid-span for some velocities. To understand the reason behind that, the dynamic bending moment (DBM) of mid-span induced by the SA5

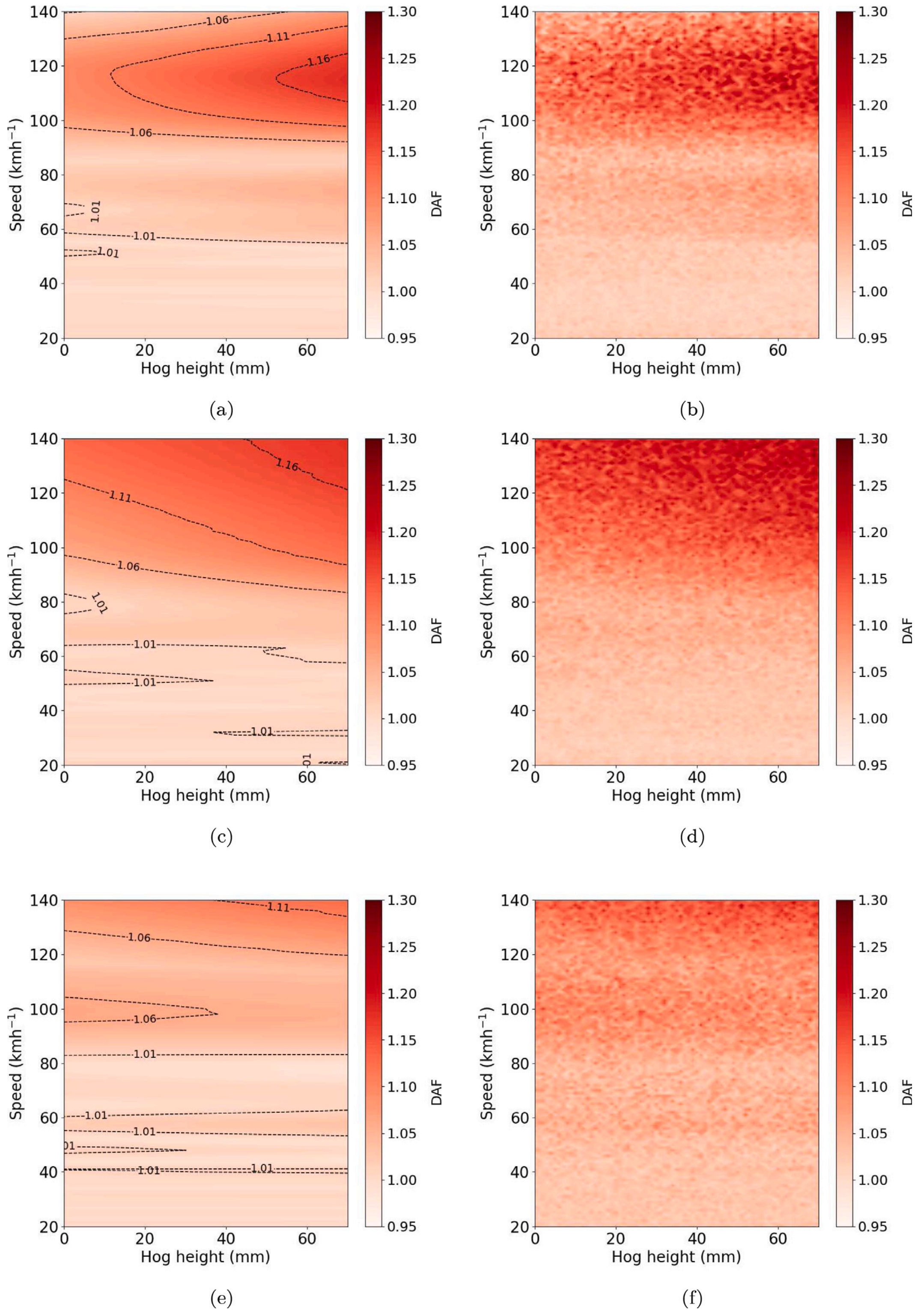

Fig. 5. DAF of 28 m simply supported bridge at mid-span, hog height vs vehicle velocity: (a) B-Double, smooth road condition; (b) B-Double, Class B road; (c) SA6, smooth road condition; (d) SA6, Class B road; (e) SA5, smooth road condition; (f) SA5, Class B road.

driving on a smooth road at speed 100 $\mathrm{km\,h^{-1}}$ is shown as an example in Fig. 6. It shows the DBM of the 28 m bridge at mid-span without hog, where the DBM is determined by the acceleration at mid-span. It can be seen that due to the configuration of SA5 vehicle, the maximum total bending moment occurs at 0.88 s, while the maximum dynamic moment is earlier, which is also the case for a 70 mm hog. Despite the maximum DBMs occurring in both cases at the same time (0.63 s), and the magnitude of the negative crest increasing from 107 134 N m to 129 428 N m, the DBM at the instance when maximum total bending moment is obtained reduces from 91 376 N m to 74 233 N m. So it seems that the hog can amplify the dynamic response of all three vehicles, but it has different effect on DAFs due to the vehicle configurations.

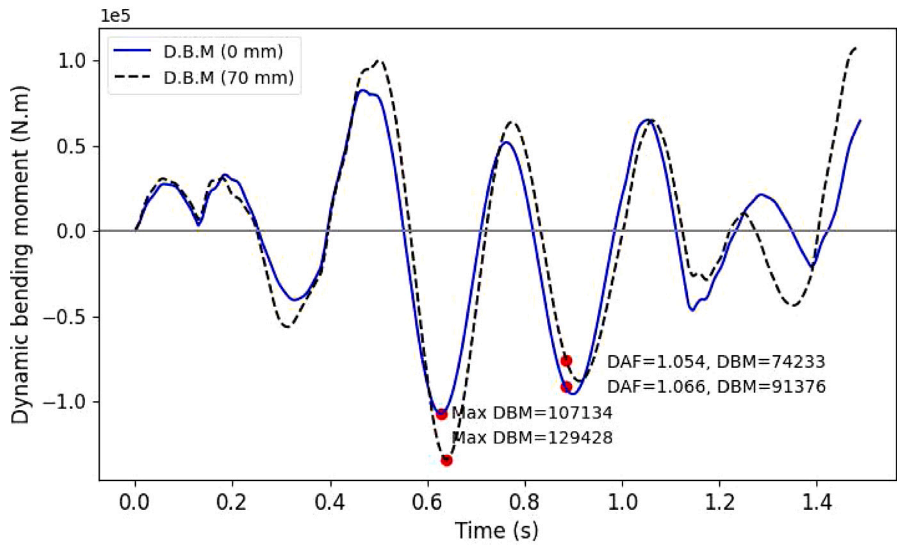

(a)

Fig. 6. Dynamic bending moments of 28 m simply supported bridge at mid-span induced by SA5 vehicle, vehicle speed = 100 $\mathrm{km\,h^{-1}}$. The solid and dashed lines represent response at: hog height = 0 mm and hog height = 70 mm. The red circles indicate the times of maximum dynamic and total bending moment.

Table 3
DAF of each span in the 15-span viaduct, with the single-span results for comparison.

Span index	B-double	SA6	SA5
Single-span	1.128	1.128	1.054
1	1.128	1.128	1.054
2	1.179	1.199	1.045
3	1.172	1.206	1.044
4	1.169	1.208	1.044
5	1.169	1.209	1.045
6	1.168	1.207	1.045
7	1.168	1.208	1.045
8	1.168	1.208	1.045
9	1.168	1.207	1.045
10	1.168	1.208	1.045
11	1.168	1.208	1.045
12	1.168	1.208	1.045
13	1.168	1.208	1.045
14	1.168	1.208	1.045
15	1.168	1.208	1.045

4.2. Span length and bridge hog

A common stock of simply-supported bridges from short- to medium-span lengths (15–40 m) is selected from [36] to investigate the dynamic behaviour of the VBI system subject to the hog, where the vehicle velocity is set to a typical highway speed of 100 $\mathrm{km\,h^{-1}}$. The results are shown in Fig. 7.

4.2.1. Result

Fig. 7(a) indicates that B-Double truck produces higher levels of DAF at short span range from 16 m to 20 m and medium span length from 28 m to 38 m, where three peaks are observed at 18 m, 20 m and 31 m. The B-Double experiences lower levels of amplification from 21 m to 25 m, with the lowest at 23 m. From Fig. 7(c), it can be seen that the DAF of the SA6 truck increases for spans from 18 m to 20 m and reaches the largest at 20 m but quickly drops to the smallest at 21 m, then it increases with the increasing span length from 21 m to 29 m. The SA5 truck produces higher levels of amplification at medium spans from 32 m to 40 m as shown in Fig. 7(e). However, the amplification caused by SA5 is slightly reduced by hogging for most spans less 32 m, especially at lower spans around 15 m to 20 m. Considering the Class B road profile results, it is clear that hogging both increases and reduces the DAF (compared to a smooth profile) at different spans, as can be seen in Figs. 7(b), 7(d) and 7(f).

4.2.2. Discussion

Larger hog of the bridge beam leads to higher levels of amplification at most of the spans for the B-Double and SA6 trucks, but lower or similar for the SA5 truck. The effect of hog on DAF is more significant at the respective critical spans for B-Double and SA6 vehicle types. For the SA5 case, DAFs ≤ 1.0 are obtained for spans 15 m to 17 m which indicates that a large dynamic moment counteracts the maximum total bending moment at the critical instant.

5. Dynamic amplification in viaducts

The viaduct is modelled as a discontinuous multi-span bridge consisting of simply-supported PSC girder bridge decks with hog as shown in Fig. 3(b). All spans are considered to have the same parameters, resulting in them having the same natural frequency. However, when considering road roughness, a random road profile is generated for each span separately, as is reasonable.

A 15-span viaduct was selected from an initial parametric study, as it has a sufficient number of spans for the DAF responses to be practically stable. Table 3 shows that the DAF of the first span in the viaduct is substantially different to that of the remaining span indices, and that the DAF becomes stable with increasing span index for each vehicle considered. In the following, we first consider the DAF of different span indices, for a fixed span length, and how it varies with vehicle speed. We then consider, for a fixed vehicle speed, the influence of span length for each span index.

5.1. Span index and vehicle speed

The numerical experiment is carried out at a range of speed from 20 $\mathrm{km\,h^{-1}}$ to 140 $\mathrm{km\,h^{-1}}$ with a 1 $\mathrm{km\,h^{-1}}$ interval on a 15-span viaduct, where the single span properties are the same as that in Section 4.1.

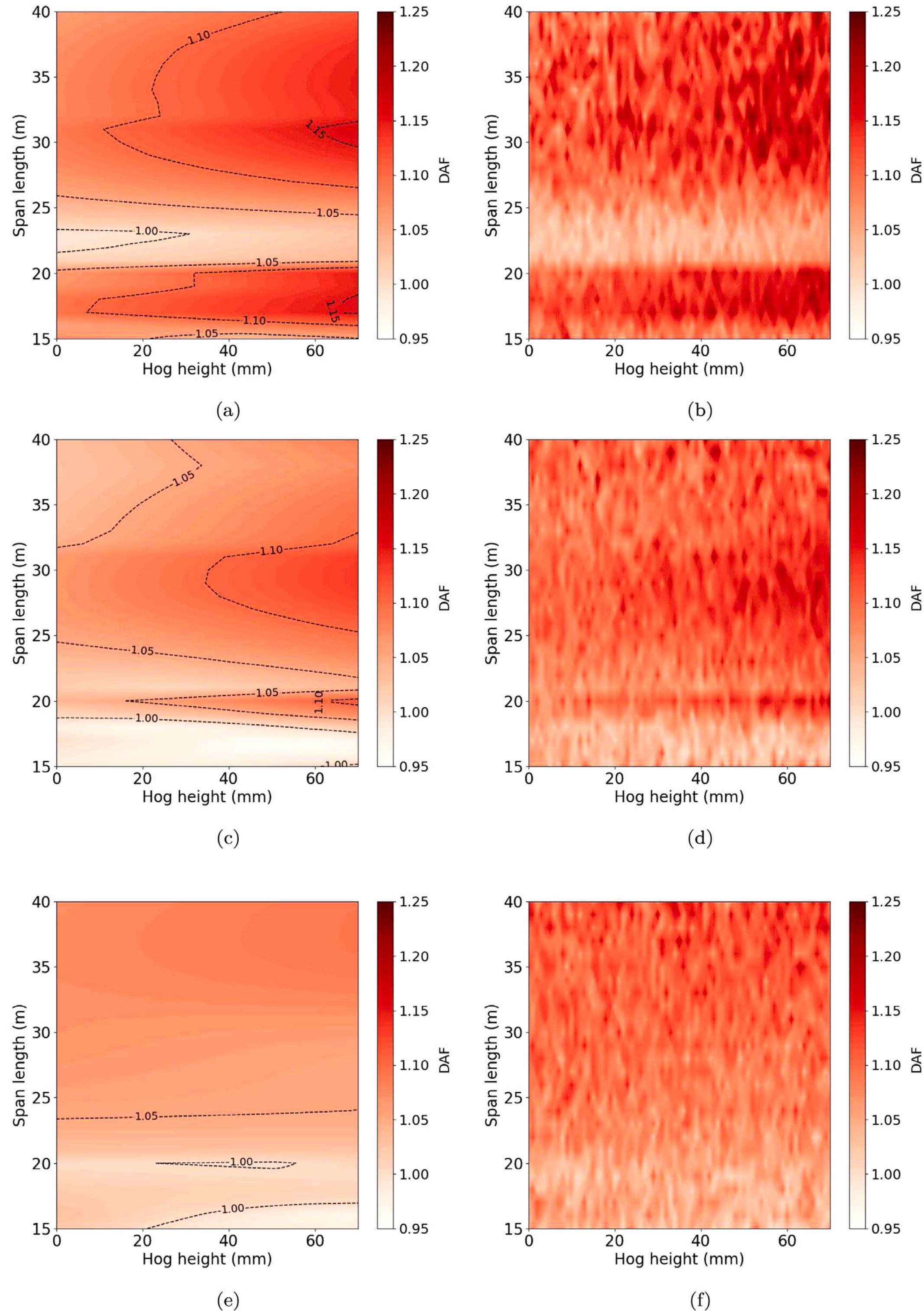

Fig. 7. DAF of simply-supported bridges from 15–40 m at mid-span, vehicle speed = 100 $\mathrm{km\,h^{-1}}$, hog height vs span length: (a) B-Double, Smooth road condition; (b) B-Double, Class B road; (c) SA6, Smooth road condition; (d) SA6, Class B road; (e) SA5, Smooth road condition; (f) SA5, Class B road.

5.1.1. Results

Fig. 8(a) suggests that the higher resonant speeds of the B-Double truck for the first span are obtained at around 73 $\mathrm{km\,h^{-1}}$ and 115 $\mathrm{km\,h^{-1}}$, while those of the remaining spans are very close to each other and occur at around 77 $\mathrm{km\,h^{-1}}$ and 124 $\mathrm{km\,h^{-1}}$. It is shown from Fig. 8(c) that the highest resonant speed of the second–fifteenth spans caused by SA6 is around 137 $\mathrm{km\,h^{-1}}$. However that critical speed of the first span exceeds 140 $\mathrm{km\,h^{-1}}$, which is out of the speed range considered. For both the B-Double and SA6 trucks, the resonant speed found at the first span is similar to that of a simply-supported bridge, and higher levels of amplification in the remaining spans are found, as compared to the simply-supported case. The highest resonant speed of SA5 occurs at around 136 $\mathrm{km\,h^{-1}}$ from the third span to the last span, while the lower critical speeds of all spans in the viaduct almost remain the same at around 95 $\mathrm{km\,h^{-1}}$ and 58 $\mathrm{km\,h^{-1}}$ as shown in Fig. 8(e). For the viaduct, Figs. 8(b), 8(d) and 8(f) indicate that the resonant speeds

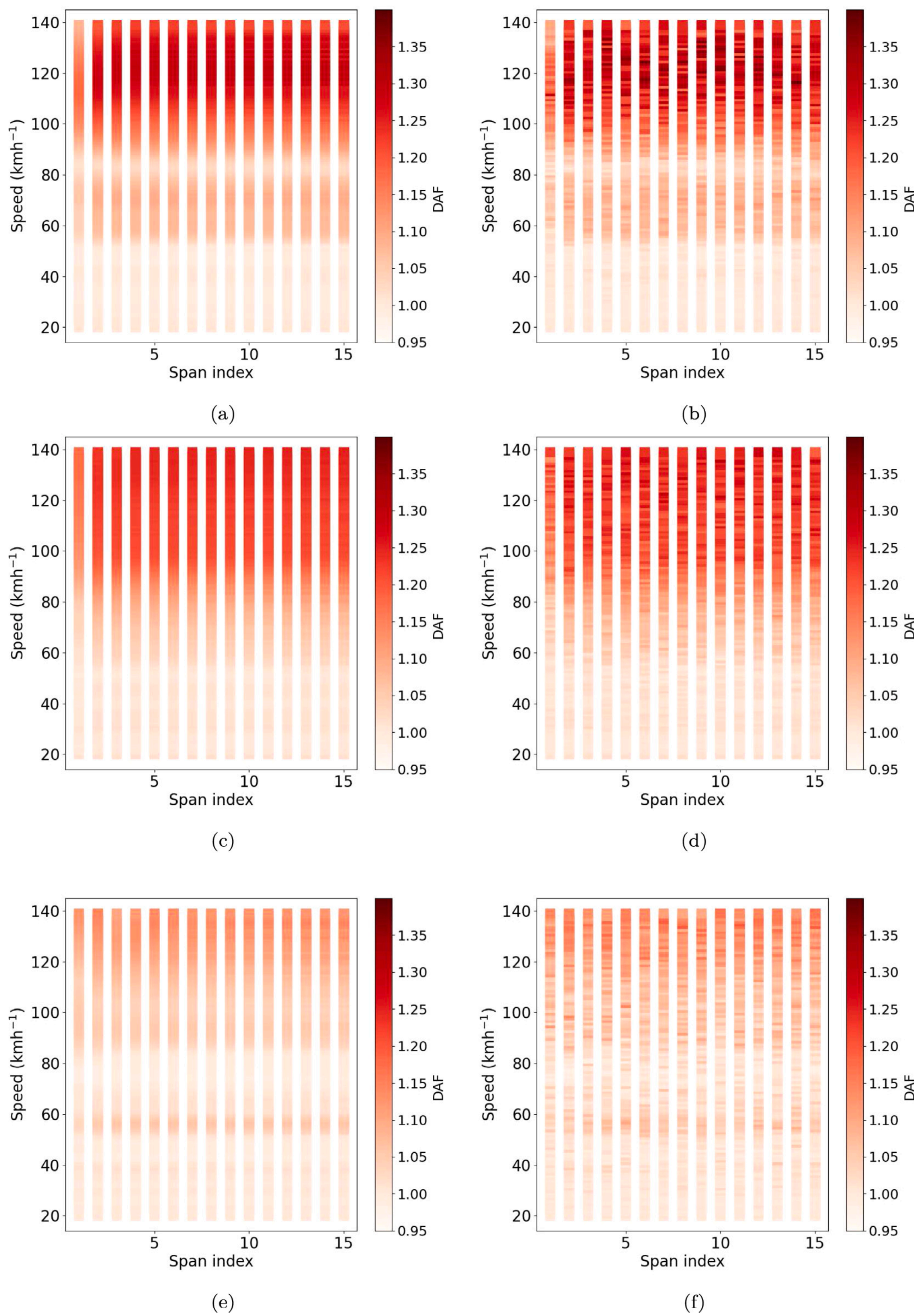

Fig. 8. DAF of a 15-span discontinuous viaduct at mid-span, span length = 28 m, hog height = 70 mm for the span index and vehicle speed: (a) B-Double, smooth road condition; (b) B-Double, Class B road; (c) SA6, smooth road condition; (d) SA6, Class B road; (e) SA5, smooth road condition; (f) SA5, Class B road.

of the three truck types can still be observed when the road roughness is considered. This is despite each span having a different road profile due to road irregularity.

5.1.2. Discussion

The results indicate that the first span in the viaduct has the same DAF as for a single-span, which may be expected. However, the DAF of subsequent spans differs substantially: for the B-Double and SA6 trucks, they are higher, whereas for the SA5 truck they are lower. The first and second spans have different DAF typically to the third–fifteenth spans. One possible reason for this behaviour is that during the time the vehicle enters a subsequent span and leaves the previous span, it not only captures an excitation caused by the previous span but also

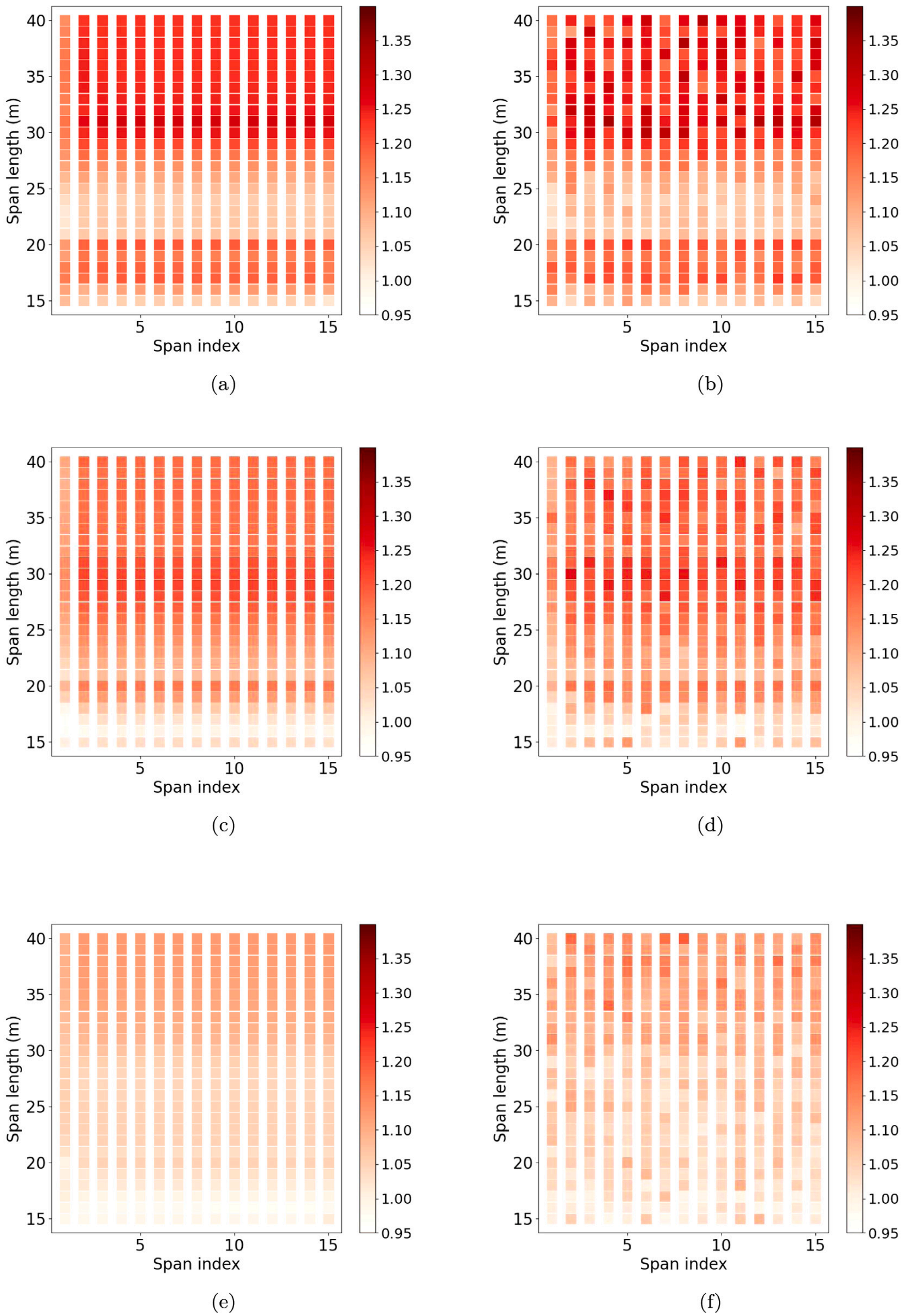

Fig. 9. DAF of a 15-span discontinuous viaduct at mid-span, hog height = $L_b/400$, vehicle speed = 100 $\mathrm{km\,h^{-1}}$, for span index and length: (a) B-Double, smooth road condition; (b) B-Double, Class B road; (c) SA6, smooth road condition; (d) SA6, Class B road; (e) SA5, smooth road condition; (f) SA5, Class B road.

interacts with both spans. This would help explain the distinction in observed DAFs between a viaduct and single-span beam.

5.2. Span index and length

The results of Section 5.1 indicate that the critical speed for a viaduct could differ to that of a single-span bridge. In this section, the vehicle speeds are kept at fairly typical highway speed of 100 $\mathrm{km\,h^{-1}}$ and the span lengths varied; all other properties are as before.

5.2.1. Results

Fig. 9(a) suggests that there is a higher amplification of the third–fifteenth spans than that of the first span in the viaduct under the B-Double truck at lengths 18 m to 40 m. Similarly, for SA6, it is seen

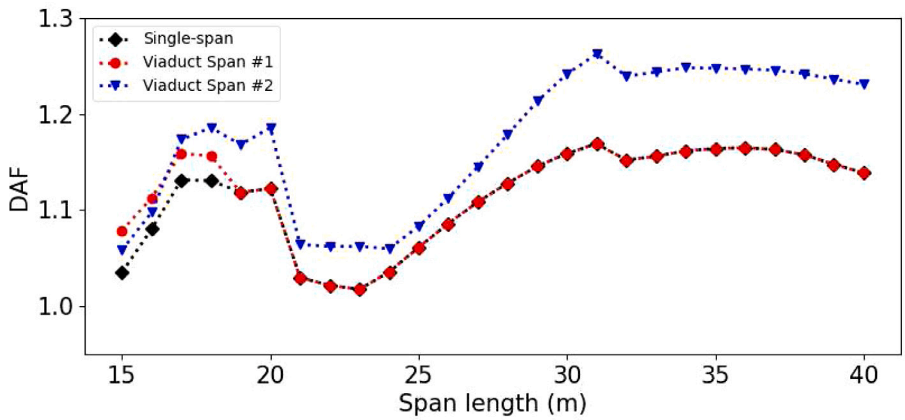

(a)

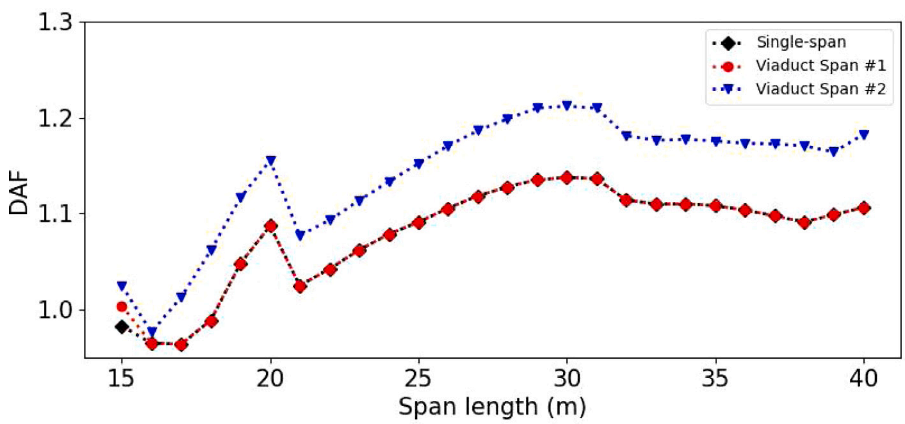

(b)

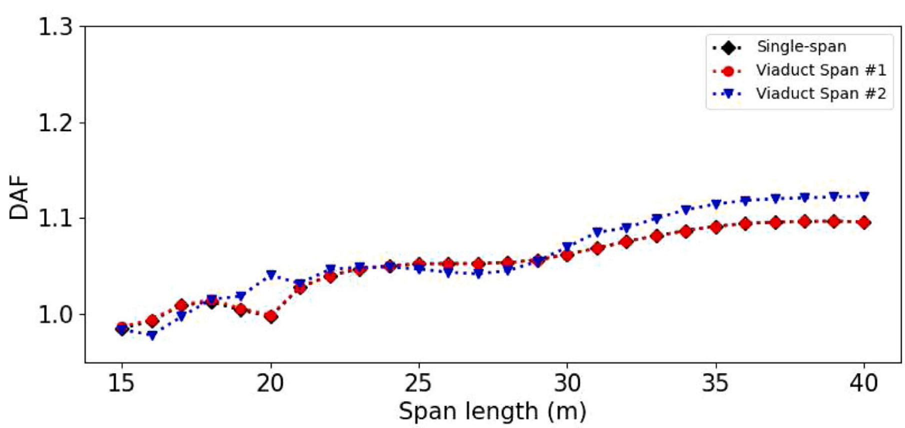

(c)

Fig. 10. Variation of DAFs of simply-supported single-span bridges and the first and second viaduct spans with span length: (a) BD vehicle ; (b) SA6 vehicle; (c) SA5 vehicle.

from Fig. 9(c) that the higher index spans produce higher DAFs than that of first span over the whole range of lengths considered. From Fig. 9(e), it is seen that for span lengths 16 m to 17 m and 25 m to 28 m, SA5 imparts lower amplifications at the 2nd–15th spans than the first span. For the three vehicles, all spans in the viaduct share a similar critical span length range, which is also similar to the single-span bridge. Once considering road roughness, the critical span lengths match well with the smooth road assumption as shown in Figs. 9(b), 9(d) and 9(f).

5.2.2. Discussion

It is shown from Figs. 9(a), 9(c) and 9(e) that the 2nd–15th spans share similar DAF results cover the whole range considered (15 m to 40 m). Therefore the amplification of the second span is selected to represent the DAF in spans other than the first span. Fig. 10(a) shows that the first span of the viaduct produces the same amplification results to the single-span case for the B-Double vehicle for span lengths from 19 m to 40 m. However, for 15 m to 18 m, the first span in the viaduct experiences higher DAFs than the single-span bridge. For SA6, from

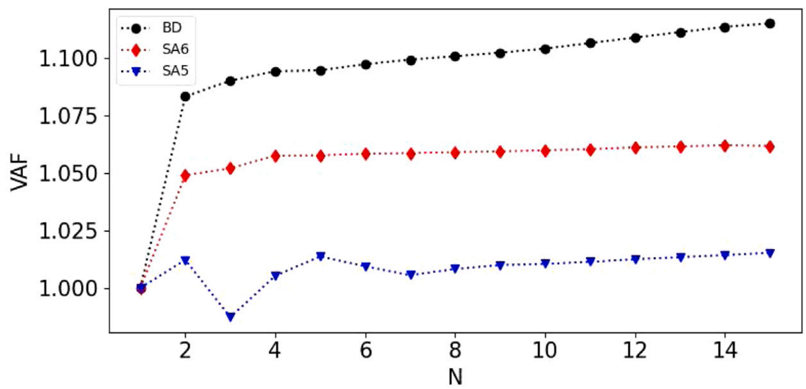

Fig. 11. The Viaduct Amplification Factor (VAF) (Eq. (45)) for N-span 28 m viaducts for the vehicles and speed range considered, for a smooth road profile.

Fig. 10(b), it can be seen that the DAF of the first span is the same as a single-span bridge over the full length range except the 15 m length. And for the SA5 truck, Fig. 10(c) shows that the first span almost has the same DAF as a single-span bridge over the lengths from 15 m to 40 m. This behaviour could be because the B-Double truck has the longest body, while SA5 is the shortest (Table 1). Nevertheless, it does seem that the second and subsequent spans in viaducts experience higher levels of dynamic amplification than equivalent single-span bridges. Indeed, this difference in DAFs is most significant at relatively higher span lengths range: 29 m to 40 m for B-Double; 17 m to 40 m for SA6; and 34 m to 40 m for SA5.

6. *N*-Span viaducts

It is shown in Section 5 that spans with higher indices experience higher amplification than the first span at most vehicle speed and span length ranges for the three vehicles considered. This indicates that the maximum DAF in any of the spans in the viaduct may increase with an increasing number of spans. To investigate the maximum DAF in any spans of the N-span viaduct, we consider fifteen viaducts of $N = 1, \dots, 15$ equal spans each and identify a *Viaduct Amplification Factor* (VAF):

$$\mathrm{VAF} = \frac{\max_{i=1}^{i=N} \mathrm{DAF}_i}{\mathrm{DAF}_{\mathrm{SS}}}, \tag{45}$$

where $\mathrm{DAF}_{\mathrm{SS}}$ is the DAF for the equivalent single-span, and DAF_i is the DAF of the ith span in a N-span viaduct.

6.1. Influence of vehicle velocity

With the same bridge properties Section 5.1, the maximum DAF of each viaduct, considering a velocity range of 20 $\mathrm{km\,h^{-1}}$ to 140 $\mathrm{km\,h^{-1}}$, is used to represent the DAF of viaducts with different numbers of spans. The VAF of Eq. (45) is shown in Fig. 11. It shows that the for the B-Double and SA6 vehicle types, that some spans in the viaduct experiences a higher DAF than an equivalent single span bridge, especially when it subjected to the B-Double heavy vehicle. Further, the maximum viaduct DAF does not increase once $N > 4$. However, viaducts subjected to SA5 experience similar or even lower levels of amplification than an equivalent single span bridge.

6.2. Influence of span length

The span length of the fifteen viaducts considered ranges from 15 m to 40 m, and the vehicle speeds of parametric vehicles are kept at 100 $\mathrm{km\,h^{-1}}$. From Fig. 12(a), it can be seen that the maximum DAF 'converges' when $N \approx 5$, and so the 5-span viaduct can sufficiently represent viaducts with a higher number of spans subjected to a B-Double truck. For SA5, Fig. 12(c) indicates that the maximum DAF 'converges' with when $N \approx 3$. Interestingly, the maximum DAF of SA6 'converges' only when the span length is from 15 m to 32 m as shown in Fig. 12(c). For span lengths over 32 m, the maximum DAF seems to continue increasing with N.

7. Conclusions

A 9-axle B-Double heavy tuck is taken as an example to demonstrate a novel approach deriving the multi-body truck by using Kane's method. Distinct from the previous vehicle model derivation methods used, the formulation based on Kane's method could be easily applied to complex types of truck and trailer combinations. With the introduction of generalized rates, the interaction forces at the joints between rigid tractor and trailers can be eliminated implicitly and automatically, leading to a straightforward derivation of the vehicle model equations. The linearized equations of motion derived by the new approach are validated with previous formulations.

This study examines the influence on dynamic amplifications of the upward camber (or hog), characteristic of many PSC girder-type bridges. The hog curve is assumed to be sinusoidal and is considered in addition to the road roughness in the dynamic system. For the simply-supported single-span bridge, the hog is found to increase the amplification induced by B-Double and SA6 vehicles, especially around the high resonant speeds and at critical span length range. In contrast, the hog has less effect on the DAF for SA5 which has a different tractor axle configuration. The reason behind the different hog effect on the three vehicles considered is likely due to the different number and weight distributions in the trailers.

Multi-span discontinuous viaducts are considered as a common form of bridge construction, especially in urban areas. We examine viaducts of up to 15 independent simply-supported spans of the same properties and hog height. Compared to single-span bridges, the DAFs induced by the B-Double and SA6 trucks on viaducts presents a different dynamic response with respect to the vehicle speed and span length. The first span in the viaduct has the similar resonant velocity to the single-span beam, while the second to fifteenth spans have similar critical speeds which differ from those of the first span in the viaduct. For 3-axle tractor vehicles like the B-Double and SA6, the second to fifteenth spans of the viaduct experience higher DAFs at mid-span compared to that of the first span and single-span bridge at most velocities. For all three vehicles, despite a similar result for DAF and span length for the first span in the viaduct and a single-span beam, the second to fifteenth spans experience a higher level of amplification compared to the single-span bridge.

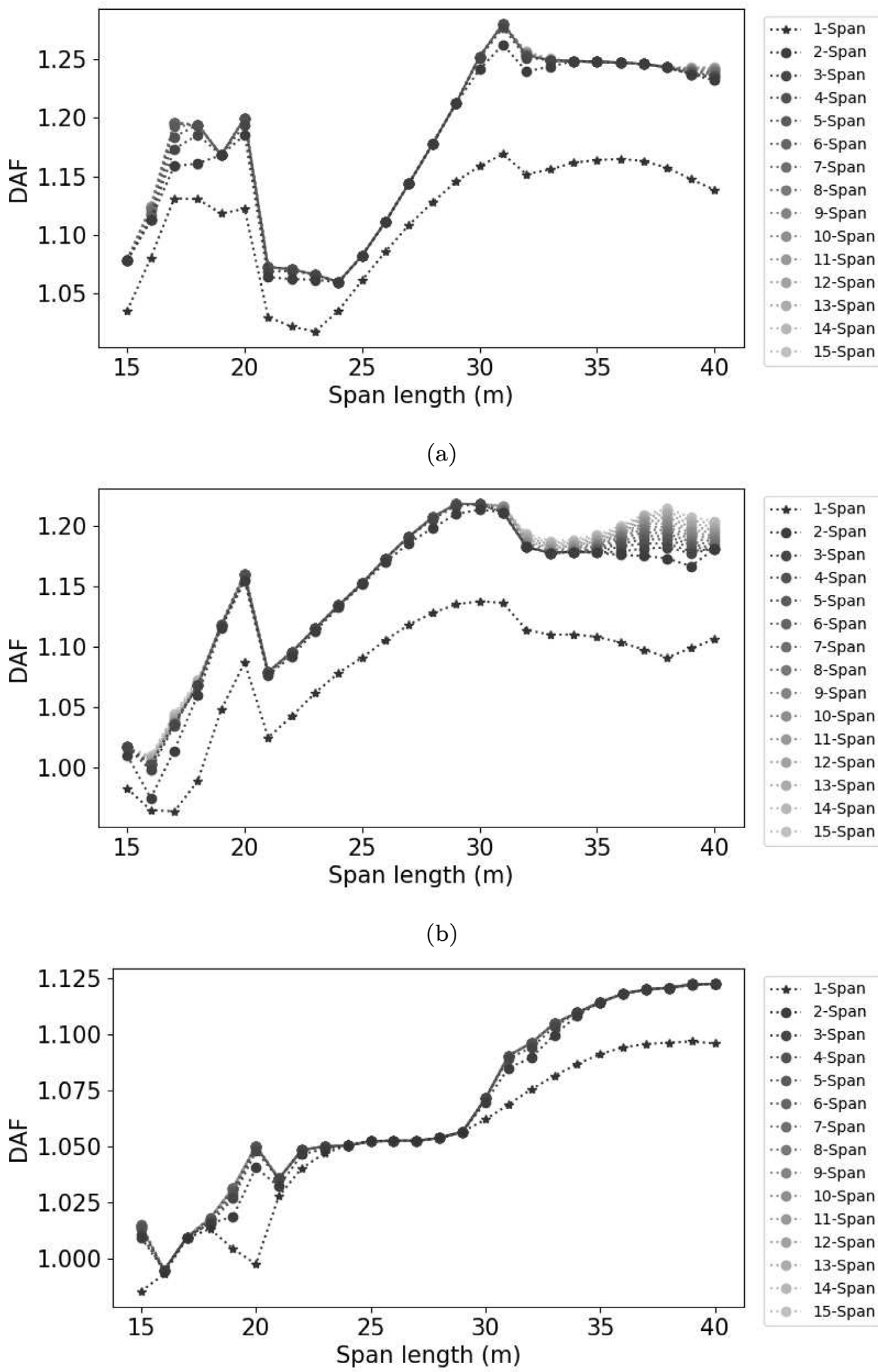

Fig. 12. DAFs of $N = 1, \ldots, 15$-span viaducts of varying span lengths for a speed of 100 $\mathrm{km\,h^{-1}}$: (a) BD vehicle; (b) SA6 vehicle; (c) SA5 vehicle.

Finally, fifteen viaducts of one to fifteen spans are investigated. For all three vehicle types, the viaduct experiences higher levels of dynamic amplification than the single span bridge. The DAF increases with increasing span numbers, but the amplification 'converges' when the span number is up to some values: five for B-Double; three for SA5. When the span length is less than 32 m, the 2-axle tractor vehicle SA6 'converges' when the span number is up to four. However, for longer span length range from 32 m to 40 m, the amplification increases with increasing span number, and more than fifteen spans may be needed to obtain the 'convergence'.

Declaration of competing interest

The authors declare that they have no known competing financial interests or personal relationships that could have appeared to influence the work reported in this paper.

Appendix A. Mass, damping and stiffness matrices of B-double vehicle

The mass matrix is expressed as:

$$\mathbf{M_v} = \begin{bmatrix} \mathbf{M_{vv}} & \mathbf{0} \\ \mathbf{0} & \mathbf{M_{GG}} \end{bmatrix}, \tag{A.1}$$

where the tractor and trailers masses associated sub-matrix $\mathbf{M_{vv}}$ and axles associated sub-matrix $\mathbf{M_{GG}}$ are described by:

$$\mathbf{M_{vv}} = \begin{bmatrix} M_{vv}^{(1,1)} & M_{vv}^{(1,2)} & M_{vv}^{(1,3)} & M_{vv}^{(1,4)} \\ & M_{vv}^{(2,2)} & M_{vv}^{(2,3)} & M_{vv}^{(2,4)} \\ & & M_{vv}^{(3,3)} & M_{vv}^{(3,4)} \\ sym. & & & M_{vv}^{(4,4)} \end{bmatrix}, \tag{A.2}$$

and

$$\mathbf{M_{GG}} = \mathrm{diag}[m_{A1}, \ldots, m_{A3}, m_{B1}, \ldots, m_{B3}, m_{C1}, \ldots, m_{C3}], \tag{A.3}$$

in which,

$$M_{vv}^{(1,1)} = M_A + M_B + M_C, \tag{A.4a}$$

$$M_{vv}^{(1,2)} = -r_1 M_B - r_1 M_C, \tag{A.4b}$$

$$M_{vv}^{(1,3)} = s_2 M_B + (s_2 - r_2) M_C, \tag{A.4c}$$

$$M_{vv}^{(1,4)} = s_3 M_C, \tag{A.4d}$$

$$M_{vv}^{(2,2)} = I_A^3 + r_1^2 M_B + r_1^2 M_C, \tag{A.4e}$$

$$M_{vv}^{(2,3)} = -r_1 s_2 M_B - r_1 (s_2 - r_2) M_C, \tag{A.4f}$$

$$M_{vv}^{(2,4)} = -r_1 s_3 M_C, \tag{A.4g}$$

$$M_{vv}^{(3,3)} = I_B^3 + s_2^2 M_B + (s_2 - r_2)^2 M_C, \tag{A.4h}$$

$$M_{vv}^{(3,4)} = s_3 (s_2 - r_2) M_C, \tag{A.4i}$$

$$M_{vv}^{(4,4)} = I_C^3 + s_3^2 M_C. \tag{A.4j}$$

The stiffness matrix is expressed as:

$$\mathbf{K_v} = \begin{bmatrix} \mathbf{K_{vv}} & \mathbf{K_{Gv}^T} \\ \mathbf{K_{Gv}} & \mathbf{K_{GG}} \end{bmatrix}. \tag{A.5}$$

The sub-matrix $\mathbf{K_{vv}}$ is defined as:

$$\mathbf{K_{vv}} = \begin{bmatrix} K_{vv}^{(1,1)} & K_{vv}^{(1,2)} & K_{vv}^{(1,3)} & K_{vv}^{(1,4)} \\ & K_{vv}^{(2,2)} & K_{vv}^{(2,3)} & K_{vv}^{(2,4)} \\ & & K_{vv}^{(3,3)} & K_{vv}^{(3,4)} \\ sym. & & & K_{vv}^{(4,4)} \end{bmatrix}, \tag{A.6}$$

in which,

$$K_{vv}^{(1,1)} = \sum_{j=1}^{3} k_{A,s}^j + \sum_{j=1}^{3} k_{B,s}^j + \sum_{j=1}^{3} k_{C,s}^j, \tag{A.7a}$$

$$K_{vv}^{(1,2)} = -\sum_{j=1}^{3} k_{A,s}^j L_A^j - r_1 \sum_{j=1}^{3} k_{B,s}^j - r_1 \sum_{j=1}^{3} k_{C,s}^j, \tag{A.7b}$$

$$K_{vv}^{(1,3)} = \sum_{j=1}^{3} k_{B,s}^j (s_2 - L_B^j) + (s_2 - r_2) \sum_{j=1}^{3} k_{C,s}^j, \tag{A.7c}$$

$$K_{vv}^{(1,4)} = \sum_{j=1}^{3} k_{C,s}^j (s_3 - L_C^j), \tag{A.7d}$$

$$K_{vv}^{(2,2)} = \sum_{j=1}^{3} k_{A,s}^j (L_A^j)^2 + r_1^2 \sum_{j=1}^{3} k_{B,s}^j + r_1^2 \sum_{j=1}^{3} k_{C,s}^j, \tag{A.7e}$$

$$K_{vv}^{(2,3)} = -r_1 \sum_{j=1}^{3} k_{B,s}^j (s_2 - L_B^j) - r_1 (s_2 - r_2) \sum_{j=1}^{3} k_{C,s}^j, \tag{A.7f}$$

$$K_{vv}^{(2,4)} = -r_1 \sum_{j=1}^{3} k_{C,s}^j (s_3 - L_C^j), \tag{A.7g}$$

$$K_{vv}^{(3,3)} = \sum_{j=1}^{3} k_{B,s}^j (s_2 - L_B^j)^2 + (s_2 - r_2)^2 \sum_{j=1}^{3} k_{C,s}^j, \tag{A.7h}$$

$$K_{vv}^{(3,4)} = (s_2 - r_2) \sum_{j=1}^{3} k_{C,s}^j (s_3 - L_C^j), \tag{A.7i}$$

$$K_{vv}^{(4,4)} = \sum_{j=1}^{3} k_{C,s}^j (s_3 - L_C)^2. \tag{A.7j}$$

The sub-matrix $\mathbf{K_{Gv}}$ is defined as:

$$\mathbf{K_{Gv}} = \begin{bmatrix} -k_{A,s}^1 & k_{A,s}^1 L_A^1 & 0 & 0 \\ \vdots & \vdots & \vdots & \vdots \\ -k_{A,s}^3 & k_{A,s}^3 L_A^3 & 0 & 0 \\ -k_{B,s}^1 & r_1 k_{B,s}^1 & k_{B,s}^1 (L_B^1 - s_2) & 0 \\ \vdots & \vdots & \vdots & \vdots \\ -k_{B,s}^3 & r_1 k_{B,s}^3 & k_{B,s}^3 (L_B^3 - s_2) & 0 \\ -k_{C,s}^1 & r_1 k_{C,s}^1 & (r_2 - s_2) k_{C,s}^1 & -k_{C,s}^1 (L_C^1 - s_3) \\ \vdots & \vdots & \vdots & \vdots \\ -k_{C,s}^3 & r_1 k_{C,s}^3 & (r_2 - s_2) k_{C,s}^3 & -k_{C,s}^3 (L_C^3 - s_3) \end{bmatrix}, \tag{A.8}$$

and the diagonal sub-matrix $\mathbf{K_{GG}}$ is defined as:

$$\mathbf{K_{GG}} = \mathrm{diag} \begin{bmatrix} k_{A,s}^1 + k_{A,t}^1 \\ \vdots \\ k_{A,s}^3 + k_{A,t}^3 \\ k_{B,s}^1 + k_{B,t}^1 \\ \vdots \\ k_{B,s}^3 + k_{B,t}^3 \\ k_{C,s}^1 + k_{C,t}^1 \\ \vdots \\ k_{C,s}^3 + k_{C,t}^3 \end{bmatrix}. \tag{A.9}$$

The damping matrix $\mathbf{C_v}$ has an identical format to stiffness matrix, and the sub-matrices $\mathbf{C_{vv}}$, $\mathbf{C_{Gv}}$ and $\mathbf{C_{GG}}$ can be derived from the corresponding stiffness matrices by substituting the corresponding damping term c for the stiffness k.

Appendix B. Mass, damping, stiffness and mode shape matrices and force vector of bridge

The mass and stiffness matrices are:

$$\mathbf{M_b} = \mathbf{I}_{(n\times n)} = \begin{bmatrix} 1 & 0 & \cdots & 0 \\ 0 & 1 & \cdots & 0 \\ \vdots & \vdots & \ddots & \vdots \\ 0 & 0 & \cdots & 1 \end{bmatrix}, \tag{B.1}$$

and

$$\mathbf{K}_{\mathbf{b}(n\times n)} = \begin{bmatrix} \omega_1^2 & 0 & \cdots & 0 \\ 0 & \omega_2^2 & \cdots & 0 \\ \vdots & \vdots & \ddots & \vdots \\ 0 & 0 & \cdots & \omega_n^2 \end{bmatrix}, \tag{B.2}$$

and the damping matrix can be developed using proportional damping, as usual.

The mode shape matrix $\mathbf{N}_b$ can distribute the contacting forces on the beam and is given by:

$$\mathbf{N}_{b(n\times 9)} = \begin{bmatrix} \phi_1(x_1) I(x_1) & \phi_1(x_2) I(x_2) & \cdots & \phi_1(x_9) I(x_9) \\ \phi_2(x_1) I(x_1) & \phi_2(x_2) I(x_2) & \cdots & \phi_2(x_9) I(x_9) \\ \vdots & \vdots & \ddots & \vdots \\ \phi_n(x_1) I(x_1) & \phi_n(x_2) I(x_2) & \cdots & \phi_n(x_9) I(x_9) \end{bmatrix}. \tag{B.3}$$

The bridge force vector $\mathbf{F_b}$ is:

$$\mathbf{F}_{b(9\times1)} = \begin{Bmatrix} W_1 - f_1(x_1,t) \\ W_2 - f_2(x_2,t) \\ \vdots \\ W_9 - f_9(x_9,t) \end{Bmatrix}. \tag{B.4}$$

Appendix C. Matrices and vectors for single span VBI system

The coupled mass, damping, and stiffness matrices are:

$$\mathbf{M_c} = \begin{bmatrix} \mathbf{M}_v & 0 \\ 0 & \mathbf{M}_b \end{bmatrix}, \tag{C.1}$$

$$\mathbf{C_c} = \begin{bmatrix} \mathbf{C}_v & \mathbf{C}_{vb} \\ \mathbf{C}_{bv} & \mathbf{C}_b + \mathbf{C}_{bb} \end{bmatrix}, \tag{C.2}$$

$$\mathbf{K_c} = \begin{bmatrix} \mathbf{K}_v & \mathbf{K}_{vb} \\ \mathbf{K}_{bv} & \mathbf{K}_b + \mathbf{K}_{bb} \end{bmatrix}, \tag{C.3}$$

in which the sub-matrices are given by:

$$\mathbf{C}_{\mathbf{bv}(n\times13)} = \begin{bmatrix} \mathbf{0}_{n\times4} & -\mathbf{N}_{n\times9}\begin{bmatrix} c_{t1} & 0 & \cdots & 0 \\ 0 & c_{t2} & \cdots & 0 \\ \vdots & \vdots & \ddots & \vdots \\ 0 & 0 & \cdots & c_{t9} \end{bmatrix} \end{bmatrix}_{n\times13}, \tag{C.4}$$

$$\mathbf{C_{vb}} = \mathbf{C}^T_{\mathbf{bv}}, \tag{C.5}$$

$$\mathbf{C}_{\mathbf{bb}(n\times n)} = \mathbf{N}\begin{bmatrix} \mathbf{N}\begin{bmatrix} c_{t1} & 0 & \cdots & 0 \\ 0 & c_{t2} & \cdots & 0 \\ \vdots & \vdots & \ddots & \vdots \\ 0 & 0 & \cdots & c_{t9} \end{bmatrix} \end{bmatrix}^T, \tag{C.6}$$

$$\mathbf{K}_{\mathbf{bv}(n\times13)} = \begin{bmatrix} \mathbf{0}_{n\times4} & -\mathbf{N}_{n\times9}\begin{bmatrix} k_{t1} & 0 & \cdots & 0 \\ 0 & k_{t2} & \cdots & 0 \\ \vdots & \vdots & \ddots & \vdots \\ 0 & 0 & \cdots & k_{t9} \end{bmatrix} \end{bmatrix}_{n\times13}, \tag{C.7}$$

$$\mathbf{K_{vb}} = \mathbf{K}^T_{\mathbf{bv}}, \tag{C.8}$$

and

$$\mathbf{K}_{\mathbf{bb}(n\times n)} = \mathbf{N}\begin{bmatrix} \mathbf{N}\begin{bmatrix} k_{t1} & 0 & \cdots & 0 \\ 0 & k_{t2} & \cdots & 0 \\ \vdots & \vdots & \ddots & \vdots \\ 0 & 0 & \cdots & k_{t9} \end{bmatrix} \end{bmatrix}^T. \tag{C.9}$$

The combined force vector is:

$$\{\mathbf{F}_c\} = \begin{Bmatrix} \mathbf{0}_{(4\times1)} \\ \mathbf{F}_v \\ [\mathbf{N}]\{\mathbf{F_b}\} \end{Bmatrix}, \tag{C.10}$$

in which

$$\mathbf{F_b} = \begin{Bmatrix} W_1 - k_{t1}r_{x1} - c_{t1}\dot{r}_{x1} \\ W_2 - k_{t2}r_{x2} - c_{t2}\dot{r}_{x2} \\ \vdots \\ W_9 - k_{t9}r_{x9} - c_{t9}\dot{r}_{x9} \end{Bmatrix}, \tag{C.11}$$

and

$$\mathbf{F_v} = \begin{Bmatrix} k_{t1}r_{x1} + c_{t1}\dot{r}_{x1} \\ k_{t2}r_{x2} + c_{t2}\dot{r}_{x2} \\ \vdots \\ k_{t9}r_{x9} + c_{t9}\dot{r}_{x9} \end{Bmatrix}. \tag{C.12}$$

References

[1] ITF. High capacity transport: Towards efficient, safe and sustainable road freight, no. 69. OECD Publishing; 2019.
[2] ATA. Truck impact chart technical advisory procedure. Australian Trucking Association; 2018.
[3] OBrien E, Nowak A, Caprani C. Bridge traffic loading: From research to practice. CRC Press; 2021.
[4] Harris NK, OBrien EJ, González A. Reduction of bridge dynamic amplification through adjustment of vehicle suspension damping. J Sound Vib 2007;302(3):471–85.
[5] Caprani CC, González A, Rattigan PH, OBrien EJ. Assessment dynamic ratio for traffic loading on highway bridges. Struct Infrastruct Eng 2012;8(3):295–304.
[6] Caprani CC. Lifetime highway bridge traffic load effect from a combination of traffic states allowing for dynamic amplification. J Bridge Eng 2013;18(9):901–9.
[7] Frỳba L. Vibration of solids and structures under moving loads, vol. 1. Springer science & business media; 2013.
[8] O'Brien EJ, McGetrick P, González A. A drive-by inspection system via vehicle moving force identification. Smart Struct Syst 2014;13(5):821–48.
[9] Meyer M, Cantero D, Lenner R. Dynamics of long multi-trailer heavy vehicles crossing short to medium span length bridges. Eng Struct 2021;247:113149.
[10] Nikkhoo A, Hassanabadi ME, Azam SE, Amiri JV. Vibration of a thin rectangular plate subjected to series of moving inertial loads. Mech Res Commun 2014;55:105–13.
[11] González A. Vehicle-bridge dynamic interaction using finite element modelling. In: Moratal D, editor. Finite element analysis. InTech; 2010.
[12] Zhu X, Law S. Dynamic load on continuous multi-lane bridge deck from moving vehicles. J Sound Vib 2002;251(4):697–716.
[13] Liu B, Wang Y-z, Hu P, Yuan Q. Impact coefficient and reliability of mid-span continuous beam bridge under action of extra heavy vehicle with low speed. J Cent South Univ 2015;22(4):1510–20.
[14] Rezaiguia A, Laefer DF. Semi-analytical determination of natural frequencies and mode shapes of multi-span bridge decks. J Sound Vib 2009;328(3):291–300.
[15] Rezaiguia A, Ouelaa N, Laefer DF, Guenfoud S. Dynamic amplification of a multi-span, continuous orthotropic bridge deck under vehicular movement. Eng Struct 2015;100:718–30.
[16] Tadros MK, Fawzy FF, Hanna KE. Precast, prestressed girder camber variability. PCI J 2011;56(1).
[17] Standards Australia. AS 5100.5-2017: Bridge design – Design of concrete bridges. Sydney: Standards Australia; 2017.
[18] Lee J-H, Lim K-M, Park C-G. Modified PCI multipliers for time-dependent deformation of PSC bridges. Adv Civ Eng 2018;2018.
[19] Honarvar E, Nervig J, Sritharan S, He W, Rouse J. Improving the accuracy of camber predictions for precast pretensioned concrete beams. 2015.
[20] Marchesiello S, Fasana A, Garibaldi L, Piombo B. Dynamics of multi-span continuous straight bridges subject to multi-degrees of freedom moving vehicle excitation. J Sound Vib 1999;224(3):541–61.
[21] Kirkegaard PH, Nielsen SR, Enevoldsen I. Heavy vehicles on minor highway bridges: dynamic modelling of vehicles and bridges. Dept. of Building Technology and Structural Engineering; 1997.
[22] Cantero D, O'Brien EJ, González A. Modelling the vehicle in vehicle–infrastructure dynamic interaction studies. Proc Inst Mech Eng K 2010;224(2):243–8.
[23] Regulator NHV. Vehicle standards guide 22 (VSG-22) requirements for tag trailers. 2019.
[24] Cantero D. VEqMon2D–equations of motion generation tool of 2D vehicles with matlab. SoftwareX 2022;19:101103. http://dx.doi.org/10.1016/j.softx.2022.101103, URL https://www.sciencedirect.com/science/article/pii/S2352711022000693.
[25] Kane TR, Levinson DA. Dynamics, theory and applications. McGraw Hill; 1985.
[26] Purushotham A, Anjeneyulu MJ. Kane's method for robotic arm dynamics: a novel approach. J Mech Civ Eng 2013;6(4):07.
[27] Pal RS. Modelling of helicopter underslung dynamics using Kane's method. IFAC-PapersOnLine 2020;53(1):536–42.
[28] Gomez ER, Arteaga IL, Kari L. Normal-force dependant friction in centrifugal pendulum vibration absorbers: Simulation and experimental investigations. J Sound Vib 2021;492:115815.
[29] Su J, Su C, Xu S, Yang X. A multibody model of tilt-rotor aircraft based on Kane's method. Int J Aerosp Eng 2019;2019.
[30] Talaeizadeh A, Forootan M, Zabihi M, Pishkenari HN. Comparison of Kane's and Lagrange's methods in analysis of constrained dynamical systems. Robotica 2020;38(12):2138–50.
[31] sympy.physics.mechanics Ducuments, https://docs.sympy.org/latest/modules/physics/mechanics/kane.html.
[32] National Heavy Vehicle Regulator. National class 2 B-double operator's guide. 2016.
[33] National Heavy Vehicle Regulator. National heavy vehicle mass and dimension limits. 2019.

[34] Cantero D, González A, OBrien EJ. Maximum dynamic stress on bridges traversed by moving loads. Proc Inst Civ Eng 2009;162(2):75–85.

[35] Mechanical vibration – Road surface profiles – Reporting of measured data, vol. 2016. Standard, Geneva, CH: International Organization for Standardization; 2016, ISO 8608:2016.

[36] Meyer MW. The characterization of the dynamic interaction between highway bridges and long, multi-trailer heavy vehicles. 2022.